



**HAL**  
open science

# Spatial organization and functions of Chk1 activation by TopBP1 biomolecular condensates

Tom Egger, Laura Morano, Marie-Pierre Blanchard, Jihane Basbous, Angelos Constantinou

## ► To cite this version:

Tom Egger, Laura Morano, Marie-Pierre Blanchard, Jihane Basbous, Angelos Constantinou. Spatial organization and functions of Chk1 activation by TopBP1 biomolecular condensates. *Cell Reports*, 2024, 43 (4), pp.114064. 10.1016/j.celrep.2024.114064 . hal-04544892

**HAL Id: hal-04544892**

**<https://hal.science/hal-04544892>**

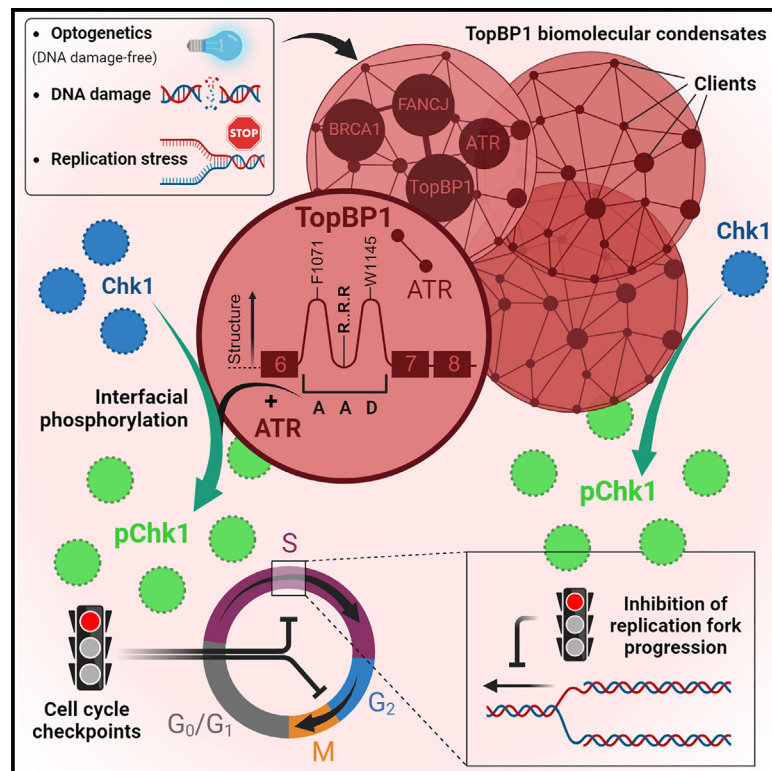
Submitted on 13 Apr 2024

**HAL** is a multi-disciplinary open access archive for the deposit and dissemination of scientific research documents, whether they are published or not. The documents may come from teaching and research institutions in France or abroad, or from public or private research centers.

L'archive ouverte pluridisciplinaire **HAL**, est destinée au dépôt et à la diffusion de documents scientifiques de niveau recherche, publiés ou non, émanant des établissements d'enseignement et de recherche français ou étrangers, des laboratoires publics ou privés.

# Spatial organization and functions of Chk1 activation by TopBP1 biomolecular condensates

## Graphical abstract



## Authors

Tom Egger, Laura Morano, Marie-Pierre Blanchard, Jihane Basbous, Angelos Constantinou

## Correspondence

jihane.basbous@igh.cnrs.fr

## In brief

Egger et al. implement their previously proposed ATR/Chk1 activation model by dissociating the functions of ATR and Chk1. Using reverse genetics and optogenetics, they show that Chk1 is phosphorylated at the interface of TopBP1 biomolecular condensates, triggering cell cycle checkpoints and slowing down replication fork progression.

## Highlights

- BRCA1 is partitioned within TopBP1 condensates in a FANCD1-dependent manner
- Chk1 is phosphorylated at the interfacial regions of TopBP1 biomolecular condensates
- Optogenetic TopBP1 condensation system recapitulates this phenomenon
- Light-activated Chk1 phosphorylation triggers cell cycle checkpoints without DNA damage



## Article

# Spatial organization and functions of Chk1 activation by TopBP1 biomolecular condensates

Tom Egger,<sup>1</sup> Laura Morano,<sup>1</sup> Marie-Pierre Blanchard,<sup>2</sup> Jihane Basbous,<sup>1,4,\*</sup> and Angelos Constantinou<sup>1,3</sup><sup>1</sup>Institut de Génétique Humaine, Université de Montpellier, CNRS, Montpellier, France<sup>2</sup>Montpellier Ressources Imageries, BioCampus, Université de Montpellier, CNRS, Montpellier, France<sup>3</sup>Deceased<sup>4</sup>Lead contact\*Correspondence: [jihane.basbous@igh.cnrs.fr](mailto:jihane.basbous@igh.cnrs.fr)<https://doi.org/10.1016/j.celrep.2024.114064>**SUMMARY**

Assembly of TopBP1 biomolecular condensates triggers activation of the ataxia telangiectasia-mutated and Rad3-related (ATR)/Chk1 signaling pathway, which coordinates cell responses to impaired DNA replication. Here, we used optogenetics and reverse genetics to investigate the role of sequence-specific motifs in the formation and functions of TopBP1 condensates. We propose that BACH1/FANCI is involved in the partitioning of BRCA1 within TopBP1 compartments. We show that Chk1 is activated at the interface of TopBP1 condensates and provide evidence that these structures arise at sites of DNA damage and in primary human fibroblasts. Chk1 phosphorylation depends on the integrity of a conserved arginine motif within TopBP1's ATR activation domain (AAD). Its mutation uncouples Chk1 activation from TopBP1 condensation, revealing that optogenetically induced Chk1 phosphorylation triggers cell cycle checkpoints and slows down replication forks in the absence of DNA damage. Together with previous work, these data suggest that the intrinsically disordered AAD encodes distinct molecular steps in the ATR/Chk1 pathway.

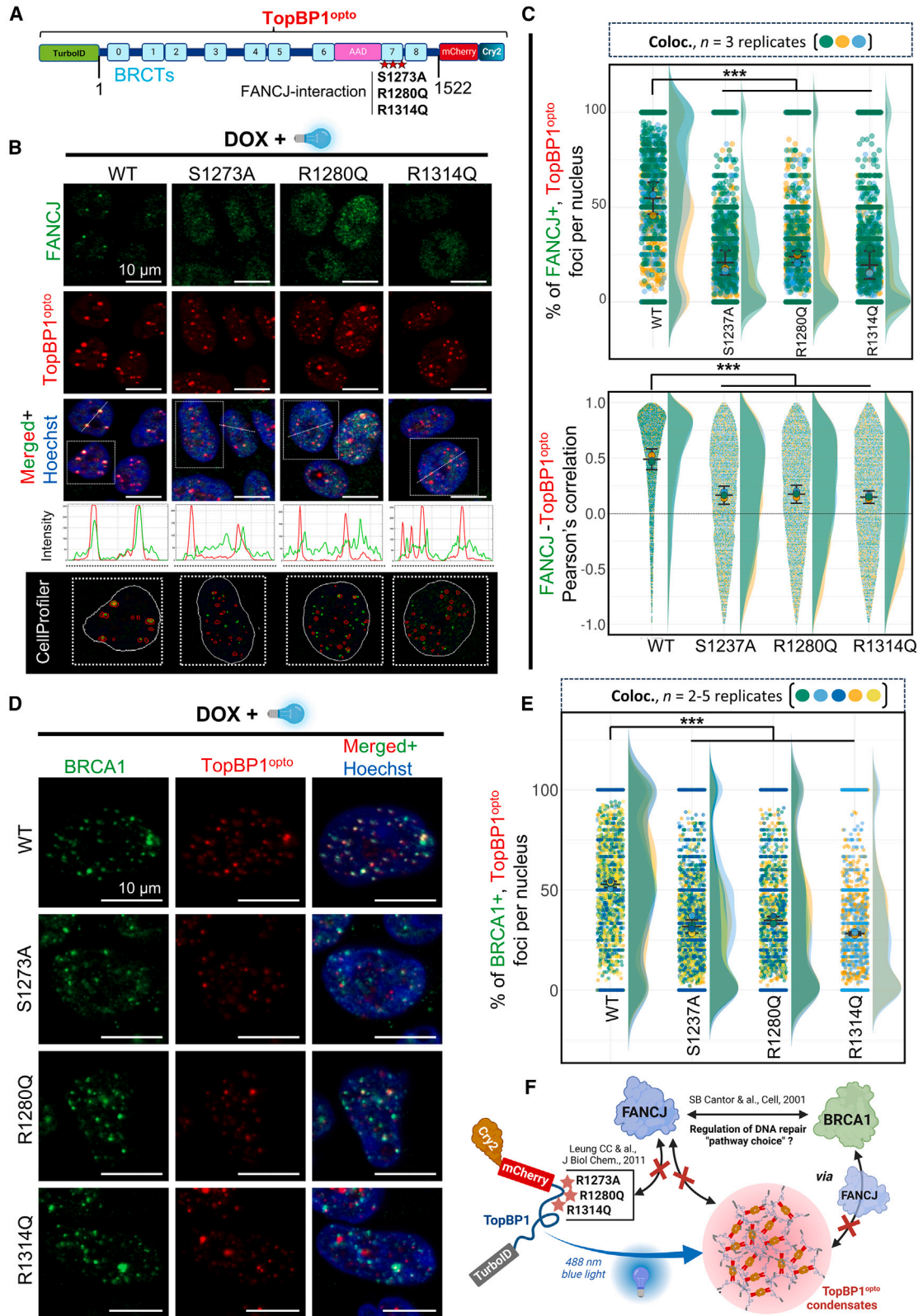
**INTRODUCTION**

The protein kinase cascades initiated by ATM/Chk2 and ATR/Chk1 coordinate the cellular response to DNA damage through phosphorylation of more than 1,000 protein substrates.<sup>1</sup> ATR/Chk1 signaling promotes the rescue of stalled forks,<sup>2</sup> the regulation of origin firing,<sup>3,4</sup> and the regulation of the dNTP pool,<sup>5,6</sup> and it activates cell-cycle checkpoints,<sup>7–13</sup> allowing time for DNA repair. ATR activation is a multistep process initiated by the regulated assembly of ATR-signaling proteins at DNA lesions or stalled and collapsed replication forks. Genotoxic stress yields RPA-covered single-stranded DNA that functions as a signaling platform sensed by ATRIP/ATR.<sup>14</sup> BACH1/FANCI promotes ATR/Chk1 signaling by unwinding G-quadruplex structures formed behind the replicative helicase that interfere with RPA binding.<sup>15,16</sup> TopBP1 is the main activator of ATR in S phase.<sup>17</sup> It is recruited to the ATR-activating structure by the MRN complex,<sup>18</sup> and is stabilized at stalled forks by interactions with RPA,<sup>19</sup> ATRIP,<sup>20</sup> and the 9-1-1 complex.<sup>21,22</sup> Next, the phosphorylation of TopBP1 by the basal kinase activity of ATR promotes the assembly of TopBP1 biomolecular condensates visualized as micrometer-sized nuclear foci by indirect immunofluorescence.<sup>23,24</sup> Importantly, the condensation of TopBP1 directly correlates with the activation by phosphorylation of the effector kinase Chk1.<sup>23,24</sup>

Macromolecular assemblies range from nanometer-sized molecular machines with defined stoichiometry to non-stoichiometric micrometer-sized structures called biomolecular

condensates that concentrate proteins and nucleic acids without a surrounding membrane. The term biomolecular condensates was coined to describe a variety of mesoscale assemblies, regardless of the molecular mechanism of assembly.<sup>25</sup> There is considerable interest in understanding how biomolecular condensates form and how the intrinsic molecular organization of the condensates determines their composition and functions to distinguish pathological and incidental condensates from those essential for cell physiology.<sup>26–28</sup> Two dominant paradigms explaining condensate formation are assembly by liquid-liquid phase separation (LLPS)<sup>25,29–31</sup> and assembly by evolutionarily conserved binding interfaces with specific contact sites.<sup>32</sup> Recent models consider biomolecular condensates as products of a multistep process that combines more than one assembly mechanism.<sup>33,34</sup> LLPS is a thermodynamic process of de-mixing that occurs spontaneously when the components of the condensate exceed their solubility limit, defined precisely by their saturation concentration. Intrinsically disordered regions (IDRs) are thought to play an important role in LLPS. In this scenario, LLPS is determined by the overall composition and pattern distribution of amino acids in the IDR that act as spacers and stickers engaged in cooperative multivalent interactions.<sup>31,35,36</sup> For example, multiple and cooperative cation- $\pi$  interactions between tyrosine and arginine residues drive the condensation of the FUS protein,<sup>37</sup> whereas blocks of charges modulated by hyper-phosphorylation either promote or inhibit the formation of cell-cycle-regulated condensates.<sup>38,39</sup>





(legend on next page)

TopBP1 is a multivalent scaffold protein containing nine folded BRCA1 C-terminal motifs as well as an ATR activation domain (AAD) that is intrinsically disordered.<sup>40</sup> While TopBP1 condensation triggers ATR/Chk1 signaling, the nature of the molecular interactions that link TopBP1 mesoscale assembly to Chk1 activation and cellular functions remains elusive.

Chk1 is activated in the vicinity of damaged DNA and is released from chromatin to transmit the signal from the DNA damage sites to the nucleus.<sup>41</sup> However, Chk1 is not retained at DNA lesions.<sup>42</sup> Therefore, it is unclear how this highly mobile protein is activated locally at DNA damage sites to regulate a variety of stress responses via the phosphorylation of downstream substrates throughout the nucleus. Chk1 triggers cell-cycle checkpoints by inactivating CDC25 protein phosphatases, which dephosphorylate and activate cyclin-dependent protein kinases.<sup>10–13,43</sup> In S phase, Chk1 inhibits the firing of excess replication origins.<sup>7</sup> It controls TopBP1 interaction with Treslin/Ticrr, which plays a critical role in the initiation of DNA replication.<sup>8,44,45</sup> In addition, it is thought that Chk1 actively slows down the progression of replication forks. However, this function of Chk1 is matter of discussion because the DNA-damage-inducing agents used to activate the checkpoint create replication roadblocks, and inhibition of the ATR/Chk1 kinases can lead to the collapse of replication forks.<sup>46</sup> Studies using yeast as a model system suggest that the acceleration of S phase in checkpoint mutants is primarily a consequence of deregulated replication initiation events<sup>2</sup> and that RAD53<sup>Chk1</sup> rather promotes the restart of replication forks after DNA damage.<sup>47,48</sup> Also, a local checkpoint mechanism may be restricted to the replisomes that encounter DNA lesions.<sup>49</sup> By contrast, analyses of DNA replication dynamics after induction of a limited number of DNA double-strand breaks suggest that activated RAD53<sup>Chk1</sup> acts *in trans* to slow down DNA chain elongation at undamaged forks.<sup>50</sup> Consistent with this, reconstitution of DNA replication with purified yeast proteins indicates that RAD53<sup>Chk1</sup> activity slows replication forks through Mrc1/Claspin phosphorylation.<sup>51</sup> Whether similar mechanisms exist in vertebrates remains to be explored. One study provides evidence that Chk1 controls the progression of replication forks in human cells exposed to the topoisomerase inhibitor camptothecin (CPT).<sup>52</sup>

To gain insight into the organization and nature of the interactions that enable TopBP1 condensates to trigger cell-cycle checkpoints, we combined optogenetics and reverse genetics

and developed a pipeline for automated analysis of fluorescence microscopy images of TopBP1 condensates. We used site-directed mutagenesis to target the intrinsically disordered AAD of TopBP1 and identified mutations that uncouple TopBP1 condensation from Chk1 activation. Collectively, the data suggest that evolutionarily conserved contact sites promote TopBP1 functions in condensation, FANCD1 recruitment, and Chk1 activation. We provide evidence that Chk1 is phosphorylated at the interface of chromatin-bound TopBP1 condensates, activating cell-cycle checkpoints and slowing down replication-fork progression.

## RESULTS

### FANCD1 promotes the partitioning of BRCA1 within TopBP1 biomolecular condensates

To investigate the importance of sequence-specific features in the composition and functions of TopBP1 condensates, we combined reversed genetics and optogenetics. Optogenetics offer the means to control the assembly of condensates with high temporal precision and in the absence of DNA damage.<sup>23,53–55</sup> We first examined FANCD1, which interacts with TopBP1 and assists the recruitment of ATR-signaling proteins at stalled forks.<sup>15,16</sup> TopBP1 amino acids S1273, R1280, and R1314 have been identified in a crystal structure as key determinants of the specific FANCD1-TopBP1 interaction.<sup>56</sup> Thus, we expressed in a doxycycline-inducible manner recombinant wild-type (WT) and mutant TopBP1 proteins (S1273A, R1280Q, or R1314Q) fused to Cry2 (for optogenetic activation), mCherry, and TurboID (a biotin ligase used to perform TurboID experiments) (Figure 1A). We first verified the loss of TopBP1<sup>opto</sup>-FANCD1 interaction by TurboID, a biotin-based proximity-labeling approach developed in our laboratory<sup>55</sup> in cells expressing TopBP1<sup>opto</sup> S1273A and R1280Q constructs (Figure S1A). As expected, both mutants showed significant decrease of FANCD1 biotinylation, confirming the loss of proximity between TopBP1<sup>opto</sup> mutants and FANCD1, especially upon light-triggered TopBP1<sup>opto</sup> condensation. We then conducted immunofluorescence analysis in which we quantified the partitioning of FANCD1 within TopBP1<sup>opto</sup> condensates induced by optogenetic activation (i.e., exposure to pulses of 488-nm light for 3 min; Figure 1B). To quantify the partitioning of client proteins within condensates in an unbiased manner across hundreds of cells, we

### Figure 1. BACH1/FANCD1 compartmentalizes BRCA1 within TopBP1<sup>opto</sup> condensates

- (A) TopBP1<sup>opto</sup> construct, including the three substitutions of interest affecting the TopBP1-FANCD1 interaction (BRCT7).  
 (B) From top to bottom: representative micrographs of light-induced TopBP1<sup>opto</sup> condensates and endogenous FANCD1 in cells expressing WT, S1273A, R1280Q, or R1314Q TopBP1<sup>opto</sup>. Line-scans intensity profiles of TopBP1<sup>opto</sup> and FANCD1 are shown. Lower panel: representative detection of the nuclei and sub-nuclear foci with CellProfiler 4.2.1 of the selected cells (white boxes).  $n = 3$ .  
 (C) Superplot analysis of  $n = 3$  biological replicates of FANCD1 colocalization with TopBP1<sup>opto</sup> condensates. Upper panel: object-based colocalization. Total number of analyzed nuclei: WT, 1,828; S1273A, 2,246; R1280Q, 2,022; R1314Q, 2,404. Lower panel: Pearson's correlation coefficient.  $n = 3 \times 2,000$  foci. \*\*\* $p < 0.001$ ; Mann-Whitney.  
 (D) Representative micrographs of light-induced TopBP1<sup>opto</sup> condensates and endogenous BRCA1 in cells expressing WT, S1273A, R1280Q, and R1314Q TopBP1<sup>opto</sup>. DNA is counterstained with Hoechst 33342 (blue channel). Scale bars: 10  $\mu\text{m}$ .  $n = 5$  (WT, S1273A, R1280Q) and 2 (R1314Q).  
 (E) Superplot analysis of BRCA1 colocalization with TopBP1<sup>opto</sup> condensates: object-based colocalization. Number of analyzed nuclei: WT, 2,898; S1273A, 3,780; R1280Q, 3,247; R1314Q, 1,578. \*\*\* $p < 0.001$ ; Mann-Whitney.  
 (F) Proposed model for FANCD1-dependent BRCA1 recruitment in TopBP1<sup>opto</sup> condensates, generated with BioRender. R1273, R1280, and R1314 are necessary for the TopBP1-FANCD1 interaction. We propose that FANCD1 participates in the direct or indirect partitioning of BRCA1 within TopBP1 condensates via these residues. Scale bars are indicated in the panels.



developed a CellProfiler 4.2.1 pipeline. As a quality control for every single picture analyzed, we set up CellProfiler to outline foci of each color as well as the Hoechst mask over the original images, as illustrated in Figure 1B (lowest panel, “CellProfiler”). In comparison with WT TopBP1<sup>opto</sup> condensates, FANCI signals within mutant TopBP1<sup>opto</sup> condensates were significantly reduced, as quantified by object-based (% of colocalizing foci) and pixel-based (Pearson’s correlation) analyses (Figure 1C). The background of endogenous FANCI signals was higher in nuclei containing mutant TopBP1<sup>opto</sup> condensates than in nuclei containing WT TopBP1<sup>opto</sup> condensates, which reflects a defect in the partitioning of endogenous FANCI into mutant TopBP1<sup>opto</sup> compartments. Line-scan intensity profiles of cross-sections further illustrate the loss of colocalization between mutant TopBP1<sup>opto</sup> condensates and endogenous FANCI (Figure 1B, intensity panel). Thus, the partitioning of FANCI within TopBP1<sup>opto</sup> condensates depends on specific amino acid contacts.

Although FANCI facilitates ATR/Chk1 signaling via the formation of RPA-coated single-stranded DNA,<sup>15,16</sup> optogenetic condensation of TopBP1<sup>opto</sup> mutant proteins defective for FANCI interaction induced robust Chk1 phosphorylation, indistinguishable from that of WT TopBP1<sup>opto</sup> upon light-induced condensation (Figure S1B). This is likely because activation of ATR/Chk1 signaling is a multistep process. Optogenetic condensation of TopBP1 mimics a late step in ATR/Chk1 signaling that bypasses the endogenous regulatory steps required to nucleate the assembly of an ATR-signaling complex in the first place. Consistent with this, quantification of RPA2 foci after pre-extraction of soluble proteins by object-based and pixel-based analyses confirmed that chromatin-bound RPA2 signals colocalized both with WT and FANCI-partitioning-defective TopBP1<sup>opto</sup> condensates (Figures S1C and S1D).

We reasoned that, upon TopBP1 condensation, FANCI might contribute to defining the composition of TopBP1 compartments. For example, BRCA1 colocalizes with TopBP1 foci, but whether BRCA1 directly interacts with TopBP1 remains elusive. By contrast, BRCA1 interacts directly with FANCI.<sup>57</sup> In comparison with WT TopBP1<sup>opto</sup> condensates, FANCI-partitioning-defective TopBP1<sup>opto</sup> condensates exhibited reduced BRCA1 signals (Figures 1D and 1E). We obtained similar results when TopBP1 condensates were induced by cellular treatment with the DNA damage inducer CPT (Figures S1E and S1F). Thus, we propose that FANCI promotes the recruitment of BRCA1 within TopBP1 compartments, as modeled in Figure 1F. Collectively, these data suggest that a non-stoichiometric protein

network held together by sequence-specific interactions underlies TopBP1 condensates.

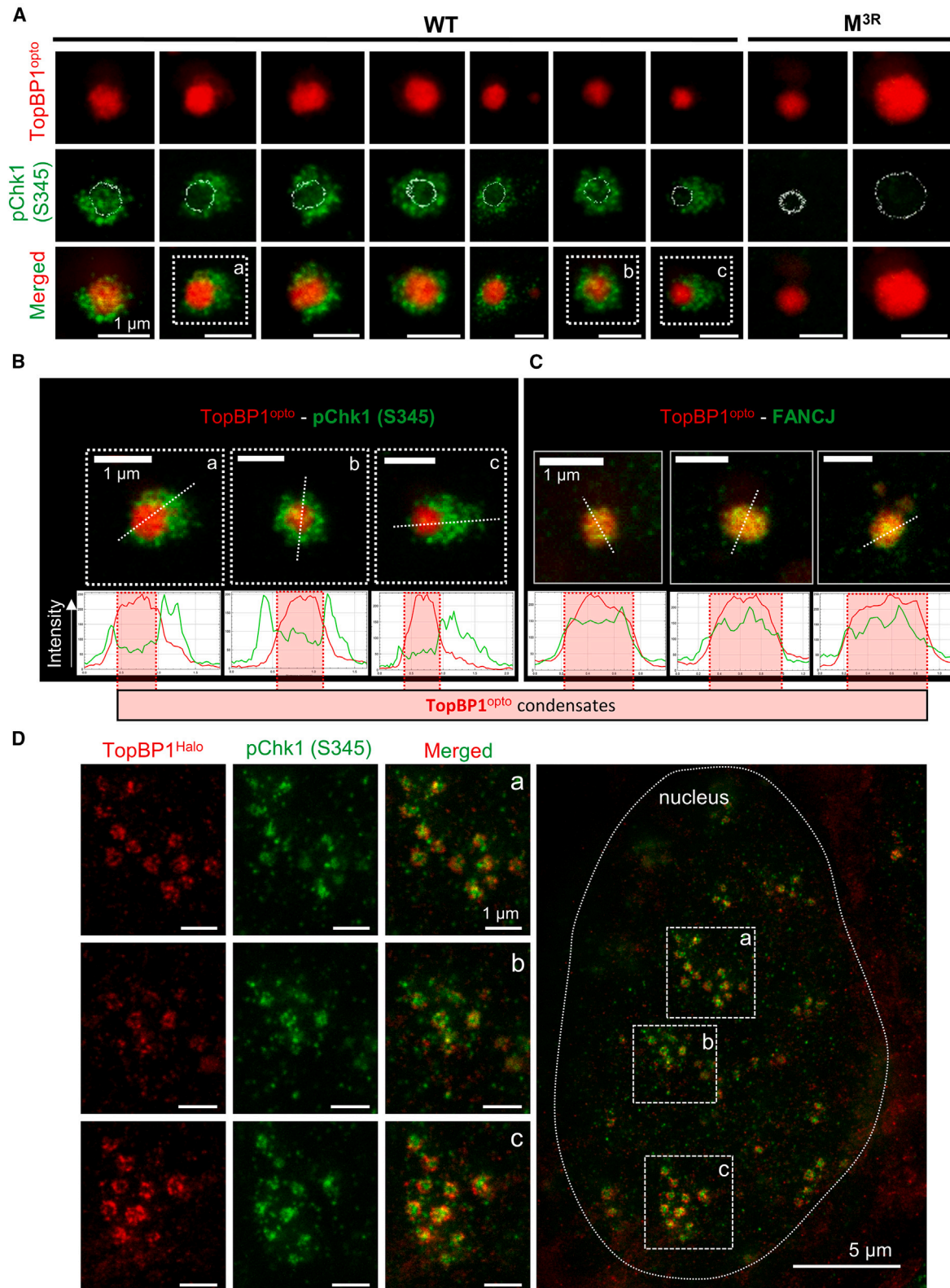
### Decoupling TopBP1 condensation from Chk1 activation

To further explore the role of sequence-specific interactions in the ATR/Chk1 signaling function of TopBP1 condensates, we performed a series of mutations in the intrinsically disordered AAD of TopBP1. Since TopBP1 phosphorylation by ATR basal kinase activity promotes TopBP1 assembly into condensates,<sup>23</sup> we reasoned that electrostatic interactions may play a role in TopBP1 condensation. We substituted with alanine potential threonine and serine phospho-sites, as well as arginine residues, which generally retain their positive charges<sup>58</sup> (Figure 2A). Contrary to our expectations, none of these mutations negatively affected TopBP1 condensation (Figures S2A and S2B). In fact, mutant TopBP1 proteins appeared to form more TopBP1 foci per nucleus than WT TopBP1 (Figure S2B). Remarkably, although optogenetic activation of WT and the M1-5 TopBP1 mutants induced Chk1 phosphorylation, the TopBP1 mutant protein carrying R1113A, R1116A, and R1118A substitutions (M<sup>3R</sup> cells thereafter) exhibited a 60% defect in light-induced Chk1 phosphorylation on serine 345, the main readout of ATR kinase activation by TopBP1 (Figures S2C and S2D). M<sup>3R</sup> cells did not show any significant alterations of two other ATR phosphorylation targets: ATR itself on threonine 1989 (T1989) and RPA2 on serine 33 (S33) (Figures S2C and S2D). In other words, upon optogenetic TopBP1 condensation, M<sup>3R</sup> cells uncouple the phosphorylation of Chk1 from TopBP1 condensation and subsequent ATR activation.

Consistent with immunoblotting analyses, pChk1 (S345) phospho-signals detected by immunofluorescence microscopy were markedly reduced in cells expressing M<sup>3R</sup> TopBP1<sup>opto</sup> (Figures 2B, 2C, and S2A). Cells that exhibit more than 15 TopBP1<sup>opto</sup> condensates showed the most profound defect in Chk1 phosphorylation (S345), as the level of pChk1 signals correlates with the number of TopBP1 condensates (Figure 2C). Furthermore, immunofluorescence experiments confirmed that the level of ATR phosphorylated on threonine 1989, an indicator of the basal kinase activity of ATR,<sup>59,60</sup> was unaffected in M<sup>3R</sup> cells (Figures 2D–2F). In fact, in comparison with cells expressing WT TopBP1<sup>opto</sup>, M<sup>3R</sup> cells showed a slight but non-significant increase in both the number of pATR (T1989) foci per nucleus (Figure 2E) and the colocalization between M<sup>3R</sup> TopBP1<sup>opto</sup> and pATR (T1989) signals (Figure 2F). We conclude that M<sup>3R</sup> TopBP1<sup>opto</sup> construct forms condensates upon optogenetic activation that accumulate active phospho-ATR (T1989) and

### Figure 2. Decoupling TopBP1 condensation from Chk1 phosphorylation

(A) Sequence alignment of the AAD of *Xenopus laevis*, *Homo sapiens*, and *Mus musculus*. Amino acid substitutions generated in this work are indicated (blue/red). (B) Representative micrographs of light-induced TopBP1<sup>opto</sup> condensates and endogenous pChk1 (S345) in cells expressing WT or M<sup>3R</sup> TopBP1<sup>opto</sup> constructs. A magnification of a single WT TopBP1<sup>opto</sup> focus surrounded by pChk1 (S345) (white box) is shown. *n* = 3. (C) Superplot analysis of pChk1 (S345) focus scoring in cells with either 0, 1–15, or >15 TopBP1<sup>opto</sup> condensates. Total number of analyzed nuclei: WT 0, 1,697; M<sup>3R</sup> 0, 947; WT 1–15, 1,293; M<sup>3R</sup> 1–15, 1,408; WT > 15, 359; M<sup>3R</sup> >15, 268. ns, non-significant, \*\*\**p* < 0.001; Mann-Whitney. (D) Representative micrographs of light-induced TopBP1<sup>opto</sup> condensates and endogenous pATR (T1989) in cells expressing WT or M<sup>3R</sup> TopBP1<sup>opto</sup>. *n* = 3. (E) Superplot analysis of pATR (T1989) focus scoring. Total number of analyzed nuclei: WT, 3,869; M<sup>3R</sup>, 3,962. ns, non-significant, Mann-Whitney. (F) Superplot analysis of pATR (T1989) colocalization with TopBP1<sup>opto</sup> condensates. Object-based colocalization. Total number of analyzed nuclei: WT, 3,847; M<sup>3R</sup>, 3,941. ns, non-significant, Mann-Whitney. Scale bars are indicated in the panels.



(legend on next page)

phospho-RPA2 (S33), yet these condensates fail to transduce the signal to Chk1.

To understand these phenotypes, we analyzed the size and the turnover of the light-induced TopBP1<sup>opto</sup> foci in M<sup>3R</sup> cells (Figures S2E–S2G). No significant difference was observed when comparing WT and M<sup>3R</sup> TopBP1<sup>opto</sup> focus size, indicating that the uncoupling between ATR and Chk1 activations in M<sup>3R</sup> cells is not due to the formation of smaller condensates (Figure S2F). The increased number of TopBP1<sup>opto</sup> foci initially observed in M<sup>3R</sup> cells ( $t = 0$  min post illumination) gradually faded over time to eventually become non-significant after 15 min post illumination, highlighting a slightly faster turnover of M<sup>3R</sup> TopBP1<sup>opto</sup> foci compared to WT (Figure S2G). However, this 15%–20% difference in the half-life of TopBP1<sup>opto</sup> foci is unlikely to account for the 60% decrease in pChk1 (S345) levels observed in M<sup>3R</sup> cells.

We next pre-incubated cells with the ATR inhibitor VE-822 before optogenetic condensation of TopBP1 (Figure S3A). Inhibition of the ATR kinase activity is known to block the assembly of TopBP1<sup>opto</sup> condensates,<sup>23</sup> and, consequently, it markedly reduced pChk1 (S345) fluorescence signals (Figure S3B). Regardless of inhibition of TopBP1 focus formation, the percentage of light-induced phospho-Chk1-positive TopBP1 foci was reduced back to the background level by the addition of VE-822 (Figure S3C). The inhibition of phospho-Chk1 on serine 345 was verified by western blotting on cells harvested from the same dishes (Figure S3D). In addition to further validating the specificity of the pChk1 (S345) immunofluorescent signals, this experiment shows that the co-occurrence of TopBP1/pChk1 structures depends on ATR kinase activity in WT cells.

To identify the mechanism that could account for the defect in the phosphorylation of Chk1 in the M<sup>3R</sup> mutants (which retain other ATR activation markers), we checked for the colocalization of WT and M<sup>3R</sup> TopBP1<sup>opto</sup> with other critical partners implicated in the activation of the ATR-Chk1 pathway, including total Chk1 itself (Figures S3E–S3G), the adaptor protein Claspin, and the initial ATR-ATRIP recruitment platform and chromatin-bound RPA2 (Figures S4A–S4C). A diffuse total Chk1 signal in optogenetically activated WT and M<sup>3R</sup> cells remained visible at sites of M<sup>3R</sup> TopBP1 condensation (Figure S3E). Total Chk1 antibody has previously been validated in immunofluorescence by small interfering RNA (siRNA) depletion.<sup>61,62</sup> Quantifications clearly indicate a depletion of phospho- (but not total) Chk1 at M<sup>3R</sup> TopBP1<sup>opto</sup> condensates (Figure S3F). This is further supported by data from biotin proximity-labeling approach showing Chk1 in proximity of light-induced TopBP1<sup>opto</sup> condensate (Figure S3G). Of note, the increased level of biotinylation of the M<sup>3R</sup> TopBP1

construct (Figure S3G) is coherent with the higher number of M<sup>3R</sup> TopBP1<sup>opto</sup> foci compared to WT (Figure S2B). In the case of Claspin, we failed to immunodetect puncta-like structures (Figure S4A) but the Pearson's correlation coefficient calculated in TopBP1<sup>opto</sup> condensates was not affected in M<sup>3R</sup> cells (Figure S4B). Surprisingly, however, both the RPA2-TopBP1<sup>opto</sup> Pearson's correlation coefficient and percentage of RPA2-positive TopBP1<sup>opto</sup> foci were found to be slightly but significantly increased in M<sup>3R</sup> cells (Figure S4C).

Collectively, these experiments demonstrate the specificity of the pChk1 (S345) immunofluorescent signal localized around TopBP1 condensates. We also show that the defective Chk1 phosphorylation observed in M<sup>3R</sup> cells is not due to a change in TopBP1 condensation characteristics (size or turnover of condensates) or to a loss of proximity between TopBP1 and Chk1 itself or the adaptor protein Claspin.

### Chk1 is phosphorylated on the surface of TopBP1 condensates

Interestingly, some pChk1 (S345) phospho-signals appeared as foci docked on the surface of WT TopBP1<sup>opto</sup> condensates (Figure 2B). Of note, as expected, the fraction of pChk1 (S345)-positive TopBP1 condensates was directly correlated with TopBP1 focus area, as a higher interfacial surface is expected to correlate with increased Chk1 phosphorylation (Figures S4D and S4E). To go further with this observation, we analyzed the organization of TopBP1 condensates and pChk1 (S345) signals using super-resolution stimulated emission depletion (STED) microscopy. STED microscopy resolves structures below the diffraction limit by the selective depletion of fluorophores to restrain the area of emission at the focal point. At super-resolution, TopBP1<sup>opto</sup> condensates appeared as dense globular clusters of nanometer-sized condensates (Figure 3A). Unlike FANCI or BRCA1, which partition within TopBP1 condensates, pChk1 (S345) signals were distributed on the surface or in close proximity to WT TopBP1<sup>opto</sup> condensates (Figure 3A). As expected, we did not detect any pChk1 (S345) signal in the proximity of mutant M<sup>3R</sup> TopBP1<sup>opto</sup> condensates (Figure 3A). Line-scan intensity profiles of cross-sections on three representative micrographs of Figure 3A confirmed the spatial organization of pChk1 (S345) signals relative to TopBP1<sup>opto</sup> condensates (Figure 3B). By contrast, super-resolution revealed an almost complete colocalization of FANCI within TopBP1<sup>opto</sup> condensates (Figure 3C).

To confirm this using a more physiological cellular model, we used a HEK293T cell line edited by CRISPR-Cas9 to express endogenous TopBP1 tagged at its carboxyl terminus with HaloTag on both alleles, namely TopBP1<sup>Halo/Halo</sup> HEK293T. We

### Figure 3. Chk1 is phosphorylated at the interfacial regions of TopBP1 condensates

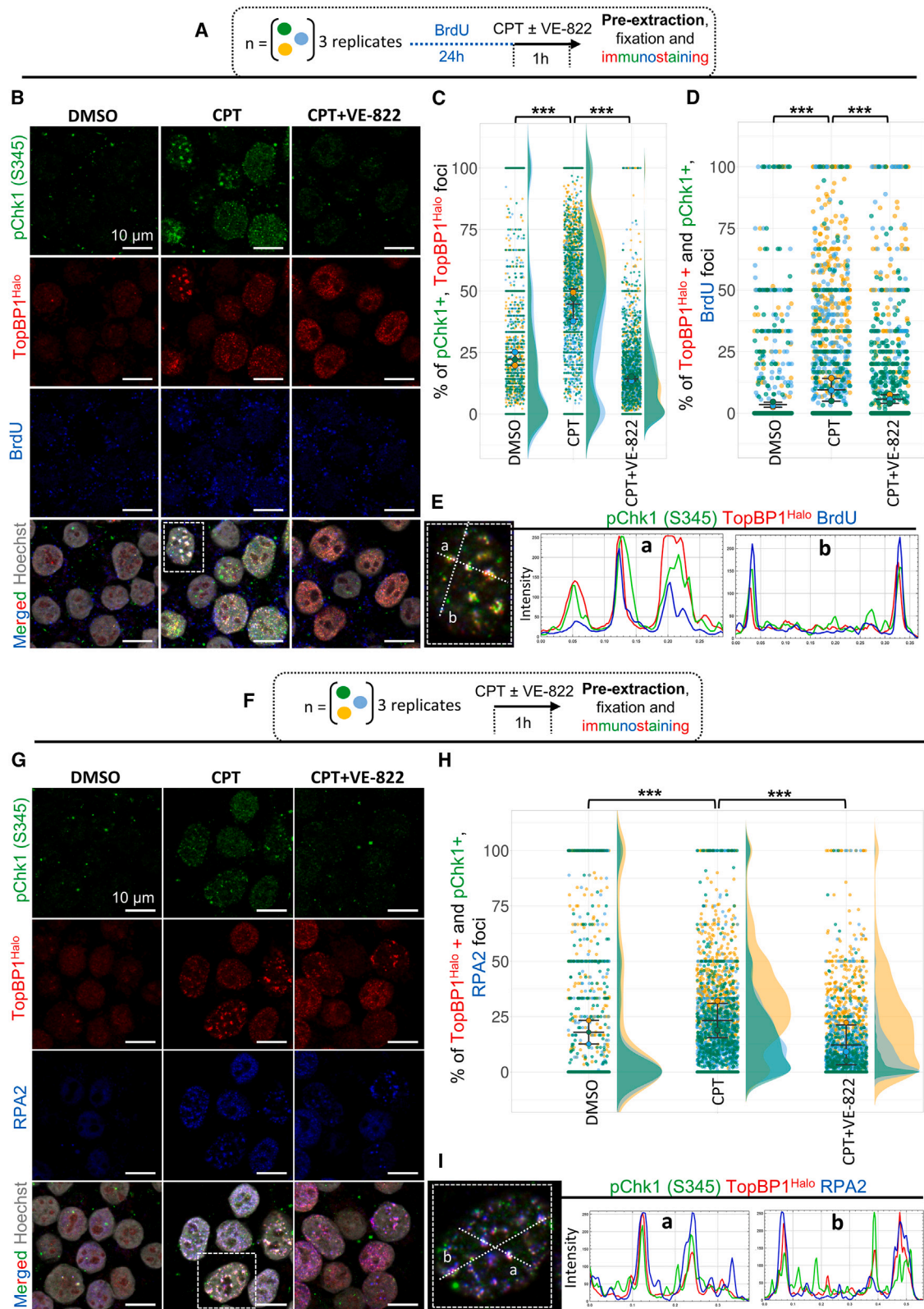
(A) Representative single midplanes STED micrographs of light-induced TopBP1<sup>opto</sup> condensates and pChk1 (S345) in cells expressing either WT or M3R TopBP1<sup>opto</sup> constructs. White dashed lines: edges of TopBP1<sup>opto</sup> condensates. White dashed square boxes (a, b, c): objects selected for line scans (Figure 3B).  $n = 3$ .

(B) Selected STED images from (A). Line-scans intensity profiles of TopBP1<sup>opto</sup> and pChk1 (S345) are shown. Edges of TopBP1<sup>opto</sup> condensates are represented by red dashed boxes.

(C) Representative STED micrographs of light-induced TopBP1<sup>opto</sup> condensates and endogenous FANCI. Line-scans intensity profiles of TopBP1<sup>opto</sup> and FANCI are shown.

(D) Representative STED micrographs of endogenous TopBP1<sup>Halo</sup> and pChk1 (S345) detected by indirect immunofluorescence in HEK293 TopBP1<sup>Halo/Halo</sup> cells exposed to CPT (1  $\mu$ M) for 1 h.

Scale bars are indicated in the panels.



(legend on next page)

induced the condensation of endogenous TopBP1 with the topoisomerase 1 inhibitor CPT and examined immuno-stained TopBP1 and pChk1 (S345) signals by STED microscopy. Interestingly, clusters of endogenous TopBP1 nano-condensates induced by CPT were smaller and less dense than recombinant TopBP1 condensates induced by optogenetic activation (Figure 3D). This is likely due to the endogenous expression level of TopBP1<sup>Halo</sup>, compared to the overexpression induced in the opto-system. Consistent with the observations made in the opto-system, phospho-Chk1 signals accumulated in close proximity to TopBP1 clusters, yet they did not colocalize with TopBP1<sup>Halo</sup> nano-condensates (Figure 3D). Although the phosphorylation of Chk1 was also detected within ring structures of TopBP1<sup>Halo</sup> (rather than at the outer boundaries in the opto-system), it remains an interfacial event. Likewise, pChk1 (S345) and TopBP1 nano-condensates exhibited similar spatial distribution patterns when TopBP1<sup>Halo</sup> was directly revealed with the HaloTag ligand Janelia Fluor 646 (Figure S5A). Collectively, these observations suggest that the highly mobile Chk1 protein is phosphorylated on the surface of TopBP1 nano-condensates.

#### Interfacial Chk1 phosphorylation around TopBP1 condensates has functional significance

To better probe the nature of these TopBP1/pChk1 (S345) structures in a model recapitulating endogenous TopBP1 expression, we performed complementary approaches in TopBP1<sup>Halo/Halo</sup> HEK293T cells to (1) study their putative chromatin binding and (2) investigate their putative localization at sites of DNA damage and replication stalling upon treatment with the DNA-damaging agent CPT (1  $\mu$ M, 1 h). A co-treatment with the ATR inhibitor VE-822 (1  $\mu$ M, 1 h) served as a negative control. During the last 15 min of drug treatment, cells were co-incubated with Janelia Fluor 554 Halo Dye to detect endogenous TopBP1<sup>Halo</sup> (red channel). We either pre-exposed the cells to 5-bromo-2'-deoxyuridine (BrdU) for 24 h before the addition of the drugs (Figure 4A) or proceeded directly to the treatments for the detection of chromatin-bound RPA2 (Figure 4F). In both cases, similar to what was performed in Figure S1C, a pre-extraction of the cytosolic compartment was performed prior to the fixation of cells, depleting the soluble fraction while allowing the specific detection of chromatin-bound, pre-extraction resistant structures.<sup>63</sup>

We were still able to detect robust pChk1 signals, especially around chromatin-bound TopBP1<sup>Halo</sup> condensates even though Chk1 is widely considered to be mostly soluble and mobile (Figures 4B and 4G). Quantification of pChk1 (S345) colocalization with TopBP1<sup>Halo</sup> showed a 2-fold increase upon CPT addition, which was completely abrogated by the co-treatment with the ATR inhibitor VE-822 (Figure 4C). The pChk1-TopBP1<sup>Halo</sup> structures also colocalized, at least partially, with the BrdU signals detected in non-denaturing conditions. This triple colocalization was enhanced by the CPT treatment and, as expected, reverted upon inhibition of ATR (Figure 4D). Representative cross-sections further confirmed the colocalization of the three entities (Figure 4E).

We confirmed these observations by co-immunodetecting chromatin-bound RPA2 (Figures 4F–4I). This strategy confirmed the location of the chromatin-bound pChk1-TopBP1<sup>Halo</sup> structures at the vicinity of replication forks stalled by CPT and labeled by the pre-extraction resistant RPA2 fraction (Figure 4H). As expected, VE-822 again completely abrogated the phenotype. Cross-sections qualitatively confirmed the colocalization of pChk1, TopBP1<sup>Halo</sup>, and RPA2 upon CPT treatment (Figure 4I).

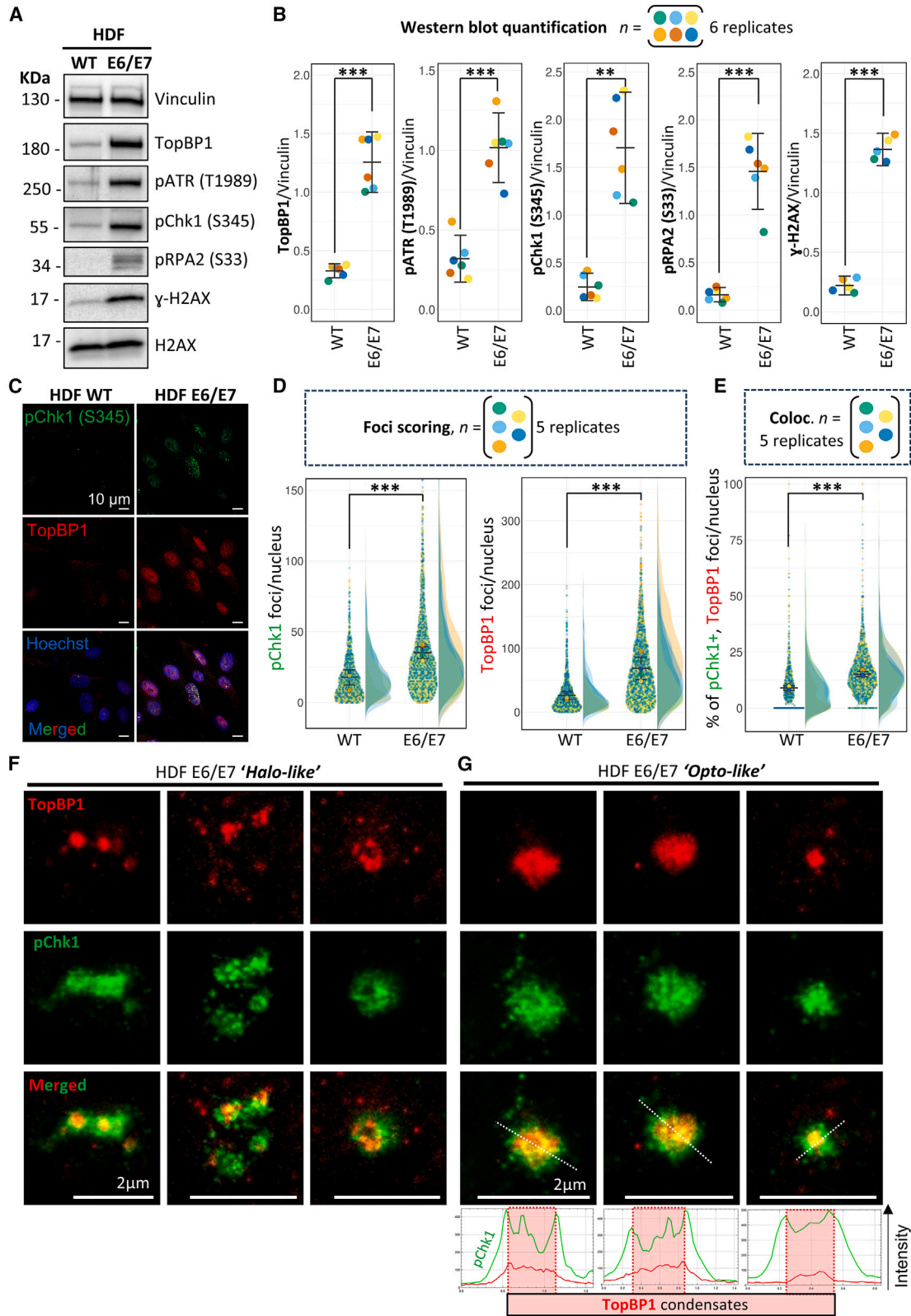
Collectively, these observations show that a significant fraction of the pChk1-TopBP1<sup>Halo</sup> structures are chromatin bound and locate at sites of DNA replication stalling upon CPT treatment.

#### Interfacial Chk1 phosphorylation around TopBP1 condensates occurs upon endogenous replication stress in primary human cells

To gain insights using a model closer to actual human physiopathology, we used primary human cells (namely human dermal fibroblasts [HDFs]) to study endogenous replication stress. We compared normally growing WT HDFs and HDFs expressing E6 and E7 oncogenes from HPV-16, as previously described.<sup>64</sup> We first assessed the activity of the ATR/Chk1 pathway by western blotting and observed that, as expected, E6/E7 HDF cells undergo a strong basal activation of the ATR-Chk1 pathway, reflecting higher levels of intrinsic replication stress (Figure 5A). We quantified fold increases ranging from 4 to 10, compared to their WT counterparts, on various ATR-Chk1 pathway markers (Figure 5B). We then performed immunofluorescence

#### Figure 4. Interfacial Chk1 phosphorylation around chromatin-bound TopBP1 condensates has functional significance

- (A) Experimental procedure for (B)–(E). HEK293 TopBP1<sup>Halo/Halo</sup> cells were pre-treated with 10  $\mu$ M BrdU for 24 h prior to drug treatments (CPT 1  $\mu$ M  $\pm$  VE-822 1  $\mu$ M, 1 h). For the last 15 min, cells were incubated with 200 nM Halo Dye JFX554.
- (B) Representative micrographs of TopBP1<sup>Halo</sup> condensates (JFX-554), immunodetected endogenous pChk1 (S345), and incorporated BrdU.  $n = 3$ .
- (C) Superplot analysis of pChk1 (S345) colocalization with TopBP1<sup>Halo</sup> condensates. Object-based colocalization. Total number of analyzed nuclei: NT, 2,866; CPT, 2,947; CPT + VE, 3,061. Tests were applied. \*\*\* $p < 0.001$ , Mann-Whitney.
- (D) Superplot analysis of pChk1 (S345) and TopBP1<sup>Halo</sup> structure colocalization with BrdU foci. Object-based colocalization. Total number of analyzed nuclei: NT, 2,496; CPT, 2,787; CPT + VE, 2,677. \*\*\* $p < 0.001$ , Mann-Whitney.
- (E) Magnification of the CPT-treated cell from the dashed white box of (B). (a and b) Line-scan intensity profiles of pChk1, TopBP1<sup>Halo</sup>, and BrdU (white dashed lines) are shown in the right panels.
- (F) Scheme of the experimental procedure for the (G)–(I).
- (G) Representative micrographs of TopBP1<sup>Halo</sup> condensates labeled with JFX554, immunodetected pChk1 (S345), and chromatin-bound RPA2.  $n = 3$ .
- (H) Superplot analysis of pChk1 (S345) and TopBP1<sup>Halo</sup> structure colocalization with RPA2. Object-based colocalization. Total number of analyzed nuclei: NT, 1,705; CPT, 2,416; CPT + VE, 2,169. \*\*\* $p < 0.001$ , Mann-Whitney.
- (I) Magnification of the CPT-treated cell from the dashed white box of (G). (a and b) Line-scan intensity profiles of pChk1, TopBP1<sup>Halo</sup>, and RPA2 (white dashed lines) are shown in the right panels.
- Scale bars are indicated in the panels.



(legend on next page)

microscopy analysis of pChk1 (S345) and TopBP1 in unchallenged fibroblasts, which revealed an increase of signal for both markers in HDF E6/E7 (Figure 5C). Specifically, we quantified significant increases of both pChk1 (S345) and TopBP1 foci per nucleus in E6/E7 (Figure 5D). The percentage of pChk1 (S345)-positive TopBP1 foci was also increased (Figure 5E). As we also detected phospho-Chk1 “ring structures” around TopBP1 foci, we completed our analysis with super-resolution (STED) microscopy on normally growing HDF E6/E7 cells (Figures 5F and 5G). Using the same sets of antibodies and similar detection settings to those used with TopBP1<sup>Halo</sup> and TopBP1<sup>Opto</sup> cells, we observed both Halo-like (Figure 5F) and Opto-like (Figure 5G) structures, revealing the interfacial occurrence of pChk1 (S345) at endogenous TopBP1 condensates. Cross-sections of the Opto-like structures highlighted local pChk1 (S345) signal enrichment at the periphery of TopBP1 condensates (Figure 5G, lower panels).

Taken together, these observations not only confirmed the reliability of the artificial TopBP1<sup>Opto</sup> system in recapitulating physiological DNA damage responses in the absence of actual DNA damage but also demonstrated that interfacial Chk1 phosphorylation at the edges of TopBP1 condensates occurs in primary human fibroblasts. Moreover, the intrinsic replication stress characterized in E6/E7-expressing HDFs was sufficient to generate such structures in the absence of any treatment with DNA-damaging agents.

### Activated Chk1 triggers a replication-fork elongation checkpoint

To study the role of Chk1 in checkpoint activation, we took advantage of the optogenetic system, which (1) avoids the confounding effect of prolonged treatments with DNA-damaging agents, and (2) allows the separation of ATR and Chk1 functions in M<sup>3R</sup> cells. Both WT and M<sup>3R</sup> TopBP1 condensates induced by optogenetic activation dissolve spontaneously within 15 min, as described in Figures S2E–S2G and previous work.<sup>23</sup> Therefore, to analyze cell-cycle checkpoints, we maintained TopBP1 condensates for 5 h by pulsing cells with 488-nm light every 10 min. We then added BrdU for 15 min and analyzed the cell-cycle distribution (Figure 6A). First, a sub-fraction of replicating cells expressing WT TopBP1<sup>Opto</sup> showed a reduced level of BrdU incorporation, a sign of replication checkpoint activation. This is visually emphasized by the red vs. green traffic lights (Figure 6A). Consistent with this, we observed a significant increase in the proportion of S-phase cells (green gate, 6% increase upon light induction) coupled to a decrease in the fraction of G<sub>0</sub>/G<sub>1</sub>

cells (pink gate, 10% decrease upon light induction) expressing WT TopBP1<sup>Opto</sup>, as quantified in Figure 6B. Furthermore, the slight increase in the G<sub>2</sub>/M coupled to the decrease in the G<sub>0</sub>/G<sub>1</sub> population in illuminated WT cells could suggest the activation of a post-replicative cell-cycle checkpoint.

To examine this putative post-replicative checkpoint, we studied the cell-cycle dynamics by performing a BrdU pulse-chase experiment. We labeled replicating cells with BrdU for 15 min before triggering the condensation of TopBP1<sup>Opto</sup> for 5 h every 10 min (Figure 6C).

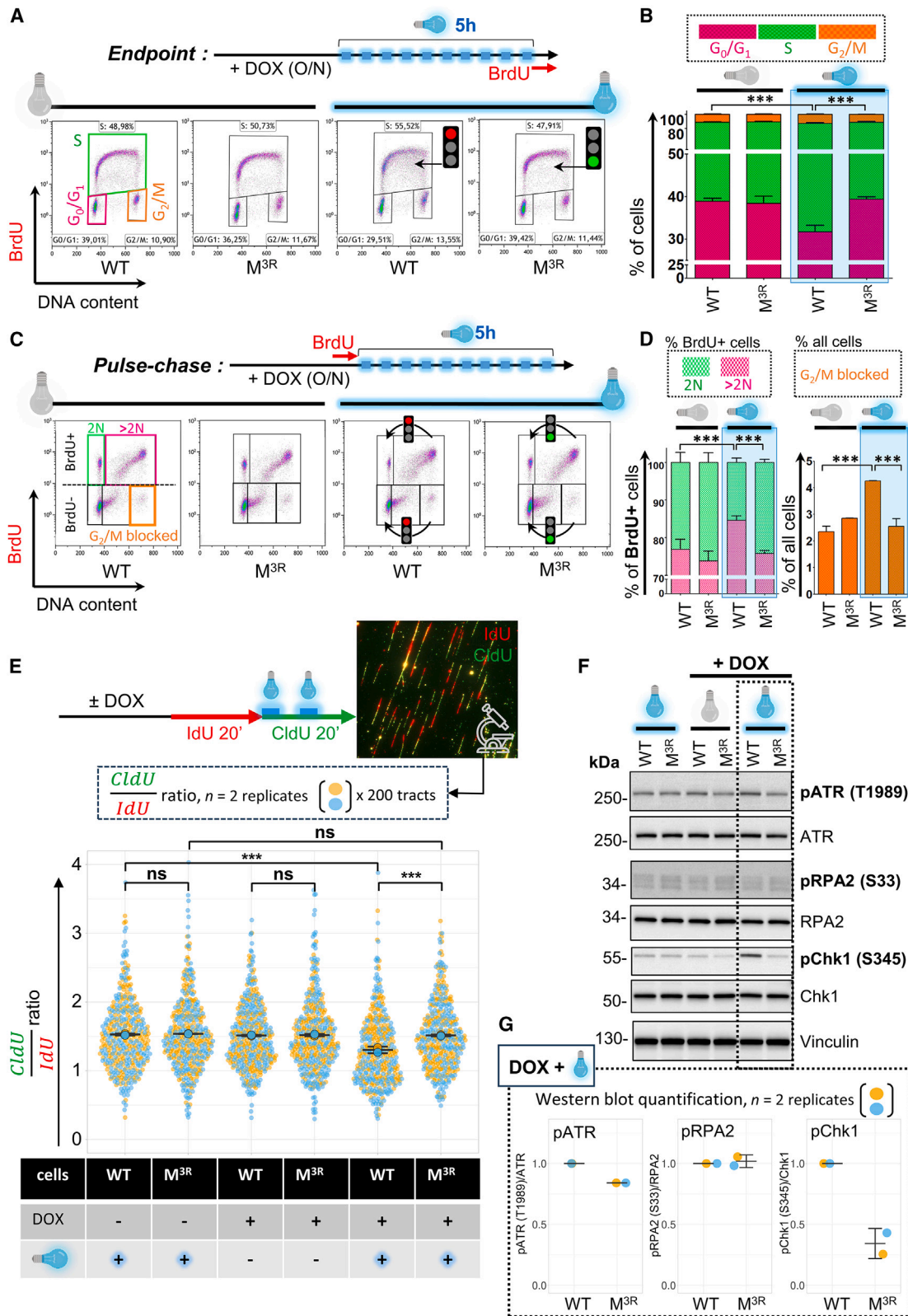
Upon TopBP1<sup>Opto</sup> condensation, WT cells accumulated in the [BrdU+, >2N] gate (pink) and partially failed to complete mitosis, as shown by the depletion in the [BrdU+, 2N] gate (green) (Figure 6D, left panel). This observation, coupled to the accumulation of the G<sub>2</sub>/M-blocked [BrdU–, 4N] gate (orange) reflects the activation of post-replicative checkpoint triggered by the condensation of WT TopBP1<sup>Opto</sup> (Figure 6D, right panel). Furthermore, this post-replicative cell-cycle checkpoint depends on Chk1, as it is not triggered in M<sup>3R</sup> cells (Figures 6C and 6D).

Together, this shows that optogenetic activation of WT TopBP1<sup>Opto</sup> induces replication and post-replicative checkpoints in the absence of the confounding effects of actual DNA damage. By contrast, condensation of the mutant M<sup>3R</sup> TopBP1<sup>Opto</sup> protein had no impact on cell-cycle dynamics. Therefore, we conclude that optogenetic TopBP1 condensates activate Chk1 to induce cell-cycle checkpoints, and that the triple arginine substitutions in the AAD of TopBP1 dissociates TopBP1 condensation from Chk1-dependent cell-cycle checkpoints.

Since optogenetic activation of WT TopBP1<sup>Opto</sup> condensation also induces the activation of the replication checkpoint (Figures 6A and 6B), we next asked whether Chk1 can regulate replication-fork elongation in the absence of DNA damage. To do so, we once again took advantage the Chk1 activation-dead mutant M<sup>3R</sup> in which we labeled newly synthesized DNA with two consecutive pulses of IdU (5-iodo-2'-deoxyuridine) and CldU (5-chloro-2'-deoxyuridine) (15 min each) while illuminating cells during the CldU pulse. We then immediately prepared DNA fibers for analysis of replication tract lengths by immunofluorescence microscopy (Figure 4E), and we harvested cells from the same dishes to quantify the activation of the ATR/Chk1 pathway by western blotting (Figures 4F and 4G). We observed a significant decrease in the CldU/IdU ratio of WT cells, induced by optogenetic activation during the second (CldU) pulse (Figure 4E), indicating that WT TopBP1 condensation slowed down the progression of replication forks. By contrast,

**Figure 5. Interfacial Chk1 phosphorylation around TopBP1 condensates occurs upon oncogene-induced replication stress in untreated primary human fibroblasts**

- (A) Immunoblot of TopBP1 and ATR-Chk1 phosphorylation targets in normally growing WT or E6/E7 HDF cells (whole-cell extracts).  $n = 6$ .  
 (B) Immunoblot quantification of  $n = 6$  independent biological replicates.  $^{**}p < 0.01$ ,  $^{***}p < 0.001$ , Welch's t tests.  
 (C) Representative micrographs of endogenous TopBP1 and pChk1 (S345) immunodetected in normally growing WT or E6/E7 HDF.  $n = 5$ .  
 (D) Superplot analysis of pChk1 (S345) and TopBP1 focus scoring. Total number of analyzed nuclei: WT, 1,474; E6/E7, 2,056.  $^{***}p < 0.001$ , Mann-Whitney.  
 (E) Superplot analysis of TopBP1-pChk1 (S345) colocalization. Total number analyzed: WT, 1,430; E6/E7, 2,036.  $^{***}p < 0.001$ , Mann-Whitney.  
 (F) Representative single midplanes STED micrographs of Halo-like endogenous TopBP1-pChk1 structures immunodetected in untreated E6/E7 HDF.  
 (G) Representative single midplanes STED micrographs of Opto-like endogenous TopBP1-pChk1 structures immunodetected in untreated E6/E7 HDF. Line-scan intensity profiles of TopBP1 and pChk1 (white dashed lines) are shown in the lower panel. Dashed red boxes represent the edges of TopBP1 condensates. Scale bars are indicated in the panels.



(legend on next page)

cells expressing the Chk1 activation-dead mutant  $M^{3R}$  TopBP1<sup>opto</sup> did not slow down replication-fork progression upon TopBP1 condensation. Analyses by immunoblotting confirmed that there was no defect in the basal kinase activity of ATR, revealed by phosphorylation of both pATR (T1989) and pRPA2 (S33), whereas pChk1 (S345) was defective (Figures 4F and 4G). These observations made in the absence of the confounding effects of DNA damage or small-molecule inhibitors support the notion that activated Chk1 slows down the progression of replication forks.

## DISCUSSION

Activation of the ATR/Chk1 signaling pathway is a multistep process initiated by the production of an ATR-activating DNA structure,<sup>14</sup> facilitated by FANCI,<sup>15,16</sup> followed by the orderly recruitment of ATR-signaling proteins at DNA lesions and stalled forks.<sup>17–22</sup> In a second stage, the basal kinase activity of ATR promotes the condensation of the ATR activator TopBP1. TopBP1 condensation then stimulates ATR kinase activity through a positive feedback loop, promoting efficient phosphorylation of Chk1.<sup>23</sup> We reported that the carboxy-terminal half of TopBP1 self-assembles to form condensates *in vitro* and in living cells and is sufficient to trigger ATR/Chk1 signaling upon condensation.<sup>23</sup> Complementary microscopy analyses revealed that TopBP1 condensates are spherical and dynamic structures that can occasionally fuse together.<sup>23</sup> However, none of these macroscopic observations provide evidence for LLPS as the underlying assembly mechanism.<sup>32,33,65,66</sup> The liquid-like properties of TopBP1 condensates, however, ensure that these structures are not solid aggregates. What we do know is that the carboxy-terminal half of TopBP1, which includes BRCT6, the intrinsically disordered AAD, and BRCT7/8, encodes the essential associative interactions required for the self-assembly of ATR-activating TopBP1 condensates.<sup>23</sup>

In this study, we provide insights into the type of interactions that underpin the functions of TopBP1. In the intrinsically disordered AAD, two evolutionary conserved amino acids, phenylalanine (F1071) and tryptophan (W1145), are essential for

ATR/Chk1 signaling,<sup>17,40</sup> and for the condensation of TopBP1<sup>23</sup> (Figure S5B). Interestingly, both F1071 and W1145 are located within a high-pLDDT region of the TopBP1 AAD domain, predicted by AlphaFold-Multimer (AF-M) to have the highest folding probability when bound to ATR (Figure S5B). Here, we identified an evolutionary conserved arginine motif (<sup>1113</sup>RSGRSR<sup>1118</sup>) that is essential for Chk1 activation by phosphorylation but not for TopBP1 condensation (namely  $M^{3R}$  mutant). In contrast to amino acids required for condensation, those three arginine residues are predicted by AF-M to remain unstructured in the ATR-TopBP1 complex (Figure S5B). Internal arginine residues in proteins are always charged.<sup>58</sup> One possibility is that these conserved positively charged residues are involved in a flexible and transient electrostatic contact required for ATR to efficiently phosphorylate Chk1 upon TopBP1 condensation.

Collectively, these data suggest that the intrinsically disordered AAD of TopBP1 encodes evolutionary conserved amino acids that establish specific contacts required for the execution of distinct molecular steps in ATR/Chk1 signaling, namely TopBP1 condensation and Chk1 activation. Because groups of charged amino acids can influence phase separation,<sup>38,39,67</sup> we have also mutated putative phospho-sites that could in principle modify the distribution of charges in the AAD, yet these substitutions had no impact whatsoever on the ATR-activating function of TopBP1.

We showed that the partitioning of FANCI to TopBP1 condensates depends on specific contacts with the C-terminal tandem BRCT7/8 domains of TopBP1 and that this specific interaction between FANCI and TopBP1 is required for the recruitment of BRCA1 to TopBP1 condensates. As the composition of TopBP1 condensates likely determines their functions, the recruitment of the FANCI and BRCA1 proteins to TopBP1 compartments at damaged sites may facilitate the repair of DNA lesions by homologous recombination, acting on the “repair pathway choice.”

Our data so far lead us to conclude that evolutionarily conserved binding interfaces with site-specific contacts direct the assembly and the composition of TopBP1 condensates. In other words, the same type of molecular interactions involved

### Figure 6. Activated Chk1 triggers cell-cycle checkpoints and inhibits replication-fork elongation in the absence of exogenous DNA damage

(A) Cell-cycle profiling of cells expressing WT or  $M^{3R}$  TopBP1<sup>opto</sup> after 5 h of continuous optogenetic activation (3 min of light pulses every 10 min). Cells were pulse labeled with BrdU (10  $\mu$ M) during the last 15 min. BrdU incorporation is plotted against DNA content. 20,000 events were analyzed per condition. G<sub>0</sub>/G<sub>1</sub>, S, and G<sub>2</sub>/M gates are shown. Red and green traffic lights symbolize the activation (red) or inactivation (green) of the replication checkpoint, visualized by the inhibition of BrdU incorporation in S-phase cells.  $n = 3$  (WT) and 2 ( $M^{3R}$ ).

(B) Bar-plot quantification of cell-cycle distribution in WT or  $M^{3R}$  TopBP1<sup>opto</sup>. Fisher's exact tests were applied (\*\* $p < 0.001$ ).

(C) BrdU pulse-chase experiments: cells were pulse labeled with BrdU for 15 min before a continuous, 5-h optogenetic activation (3 min of light pulses every 10 min). The level of BrdU incorporation is plotted against DNA content. 20,000 events were analyzed per condition. BrdU-positive (BrdU+) cells were in S phase during the BrdU pulse and are subdivided into 2N (green) and >2N (pink) DNA content. 2N (green) cells have completed mitosis and display a 2N DNA content after the chase. >2N (pink) cells have not yet completed mitosis (S–G<sub>2</sub>/M state) after the chase. Cells that are in the orange G<sub>2</sub>/M-blocked gate were already in G<sub>2</sub>/M during the BrdU pulse. Red and green traffic lights symbolize the activation (red) or inactivation (green) of the post-replicative checkpoint in illuminated WT and  $M^{3R}$  cells, respectively.  $n = 2$ .

(D) Left: quantification of the percentage of 2N (green) vs. >2N (pink), BrdU-positive cells after the indicated treatments. Right: quantification of the percentage of G<sub>2</sub>/M-blocked cells (orange gates). Fisher's exact tests were applied (\*\* $p < 0.001$ ).

(E) DNA fiber analysis of replication tracts labeled with two sequential 15-min pulses of IdU and CldU. When indicated, two 3-min pulses of 488-nm blue light were applied during the CldU pulse. The dot plot represents the CldU/IdU ratio of individual replication tracts (CldU followed by IdU). Data are pooled from  $n = 2$  biological replicates. A total of 2  $\times$  200 replication tracts were analyzed per condition. ns, non-significant; \*\* $p < 0.001$ , Mann-Whitney.  $n = 2$ .

(F) Immunoblotting, with the antibodies indicated, of whole-cell extracts of cells harvested from the same dishes as used for (E).  $n = 2$ .

(G) Quantification of pATR (T1989), pRPA2 (S33), and pChk1 (S345) in the WT and  $M^{3R}$  doxycycline (DOX) + light condition for the  $n = 2$  biological replicates corresponding to the DNA fibers experiment.

in the formation of nanometer-sized protein complexes can explain the assembly of this much larger TopBP1 mesoscale structure required for its ATR-activating function. Thus, a network of protein and nucleic acids most likely underlies the molecular organization of TopBP1 condensates. Although we are not in favor of an LLPS hypothesis that would imply that TopBP1 assembles compartments through loss of solubility past its saturation concentration, some form of segregative transition between the TopBP1 network and other macromolecules and subcellular structures most likely occurs spontaneously simply because the cell is a liquid-like crowded environment.<sup>34,68,69</sup> A segregated network model is compatible with the liquid-like behavior of TopBP1 condensates.

Using high-resolution STED microscopy, we have shown that the spherical and homogeneous TopBP1 foci are in fact tight clusters of nanometer-sized condensates.<sup>23</sup> Here we observed that pChk1 (S345) clusters on (or near) the surface of TopBP1 clusters of nano-condensates, notably at sites of fork stalling and DNA damage. This spatial organization contrasts with that of FANCDJ, which colocalizes almost completely with TopBP1 condensates at super-resolution. In the context of primary human fibroblasts (HDFs) with oncogene expression as the only source of DNA replication stress, endogenous TopBP1 formed similar clusters, albeit less dense than recombinant TopBP1 clusters induced by optogenetic activation. In the physiological context of HDFs, clusters of endogenous TopBP1 and pChk1 were more intermingled yet also exhibited interfacial spatial distribution. These observations suggest that Chk1 is activated locally when it transiently contacts the surface of TopBP1 condensates prior to signal transduction throughout the nucleus. Liquid-liquid interfaces facilitate biochemical reactions, a characteristic feature that is exploited in synthetic biochemistry.<sup>70</sup> For example, it has recently been shown that the physicochemical properties of the interface of biomolecular condensates can drive redox reactions.<sup>71</sup> Protein organization and charges at the surface of condensates may contribute to the positioning of reactants, thereby facilitating biochemical reactions.

Although TopBP1 interaction with ATR is required for TopBP1 condensation and downstream activation of Chk1, the M<sup>3R</sup> TopBP1 mutant protein decouples TopBP1 condensation from Chk1 phosphorylation. Because M<sup>3R</sup> cells maintain other ATR-dependent phosphorylations and specifically fail to transduce the signal to Chk1, this system provided insights into the consequences of the sequential ATR/Chk1 signal transduction. Indeed, while the involvement of the ATR/Chk1 pathway in the S and G<sub>2</sub>/M checkpoints is well established, we show here that activated Chk1, but not ATR, induces distinct S and G<sub>2</sub>/M cell-cycle checkpoints in the absence of any exogenous DNA-damaging agent. Strikingly, consistent with our findings, Yan et al.<sup>72</sup> recently reported that cells expressing clinically relevant TopBP1 variants exhibited similar phenotypes. Of note, two frameshift variants partially or totally lacking the AAD domain showed impaired Chk1 phosphorylation and G<sub>2</sub>/M cell-cycle checkpoint upon MMS-induced DNA damage. We go further and show that the inhibition of BrdU incorporation observed in WT S-phase cells subjected to TopBP1 condensation is associated with the activation of a Chk1-dependent replication-fork elongation checkpoint,

without the ambiguity associated with the use of DNA-damaging agents, RNA interference, or inhibitory molecules. In summary, our study improves our current functional understanding of the stepwise activation of the ATR/Chk1 pathway, a cornerstone of the replication stress response.

### Limitations of the study

Endogenous TopBP1 is still expressed in the opto-system. The putative interaction between TopBP1<sup>opto</sup> and TopBP1<sup>endo</sup> may therefore limit the penetrance of the phenotypes observed with the various recombinant constructs described.

The BRCA1 recruitment within TopBP1 condensates mediated by FANCDJ could be indirect, although direct interactions between TopBP1-FANCDJ<sup>56</sup> and FANCDJ-BRCA1<sup>57</sup> are clearly established in the literature. This point could be assessed through the generation of a FANCDJ mutant defective in BRCA1 binding but proficient in TopBP1 condensate localization. If such a mutant failed to recruit BRCA1 within TopBP1 condensates, it would provide valuable insights into the specific interactions governing BRCA1 recruitment into TopBP1 condensates.

The HEK293 Flp-In system inherently manifests a moderate degree of endogenous replication stress, rendering the execution of precise single-DNA-lesion analyses challenging. Nevertheless, experiments conducted in the HDF model for the comprehensive study indicate that the distinctive Chk1 phosphorylation pattern at the periphery of TopBP1 condensates is also observable in a physiologically relevant cellular context.

### STAR★METHODS

Detailed methods are provided in the online version of this paper and include the following:

- KEY RESOURCES TABLE
- RESOURCE AVAILABILITY
  - Lead contact
  - Materials availability
  - Data and code availability
- EXPERIMENTAL MODEL AND STUDY PARTICIPANT DETAILS
- HUMAN CELL LINES
  - Human cell lines
- METHOD DETAILS
  - Generation of mutant Opto-TopBP1 plasmids
  - Treatments
  - Antibodies
  - Immunofluorescence
  - CellProfiler 4.2.1 pipelines
  - STED microscopy
  - Western blotting
  - TurboID proximity assay
  - DNA fiber assay
  - Flow cytometry
- QUANTIFICATION AND STATISTICAL ANALYSIS

### SUPPLEMENTAL INFORMATION

Supplemental information can be found online at <https://doi.org/10.1016/j.celrep.2024.114064>.

## ACKNOWLEDGMENTS

In memory of A.C., whose significant contribution to the field of DNA damage response will remain an enduring source of inspiration for our research. We acknowledge the national infrastructure France-Bioluming supported by the French National Research Agency (ANR-10-INBS-04) and Sophie Vidal-Eychenié for technical help. This work was supported by the French National Cancer Institute INCa (PLBIO 2021), by the French Agence Nationale de la Recherche ANR (AAPG2021), and by the Fondation MSD AVENIR. We thank James R.A. Hutchins for his help with manuscript proofreading and Hervé Seitz for his help with statistics. BioRender was used to generate the graphical abstract.

## AUTHOR CONTRIBUTIONS

Conceptualization, T.E., L.M., and A.C.; methodology, T.E., L.M., and J.B.; formal analyses, T.E. and L.M.; investigation, T.E., L.M., M.-P.B.; STED acquisition, T.E., L.M., and J.B.; writing – original draft, T.E. and A.C.; writing – review & editing, T.E., L.M., J.B., and A.C.; visualization, T.E. and L.M.; supervision, J.B. and A.C.; project administration, A.C.; funding acquisition, A.C.

## DECLARATION OF INTERESTS

The authors declare no competing interests.

Received: October 3, 2023

Revised: February 14, 2024

Accepted: March 21, 2024

## REFERENCES

- Matsuoka, S., Ballif, B.A., Smogorzewska, A., McDonald, E.R., 3rd, Hurov, K.E., Luo, J., Bakalarski, C.E., Zhao, Z., Solimini, N., Lerenthal, Y., et al. (2007). ATM and ATR substrate analysis reveals extensive protein networks responsive to DNA damage. *Science* 316, 1160–1166.
- Tercero, J.A., and Diffley, J.F. (2001). Regulation of DNA replication fork progression through damaged DNA by the Mec1/Rad53 checkpoint. *Nature* 412, 553–557.
- Ge, X.Q., Jackson, D.A., and Blow, J.J. (2007). Dormant origins licensed by excess Mcm2-7 are required for human cells to survive replicative stress. *Genes Dev.* 21, 3331–3341.
- Ibarra, A., Schwob, E., and Méndez, J. (2008). Excess MCM proteins protect human cells from replicative stress by licensing backup origins of replication. *Proc. Natl. Acad. Sci. USA* 105, 8956–8961.
- D'Angiolella, V., Donato, V., Forrester, F.M., Jeong, Y.T., Pellacani, C., Kudo, Y., Saraf, A., Florens, L., Washburn, M.P., and Pagano, M. (2012). Cyclin F-mediated degradation of ribonucleotide reductase M2 controls genome integrity and DNA repair. *Cell* 149, 1023–1034.
- Zhang, Y.-W., Jones, T.L., Martin, S.E., Caplen, N.J., and Pommier, Y. (2009). Implication of checkpoint kinase-dependent up-regulation of ribonucleotide reductase R2 in DNA damage response. *J. Biol. Chem.* 284, 18085–18095.
- Petermann, E., Woodcock, M., and Helleday, T. (2010). Chk1 promotes replication fork progression by controlling replication initiation. *Proc. Natl. Acad. Sci. USA* 107, 16090–16095.
- Guo, C., Kumagai, A., Schlacher, K., Shevchenko, A., Shevchenko, A., and Dunphy, W.G. (2015). Interaction of Chk1 with Treslin negatively regulates the initiation of chromosomal DNA replication. *Mol. Cell* 57, 492–505.
- Heffernan, T.P., Ünsal-Kaçmaz, K., Heinloth, A.N., Simpson, D.A., Paules, R.S., Sancar, A., Cordeiro-Stone, M., and Kaufmann, W.K. (2007). Cdc7-Dbf4 and the human S checkpoint response to UVC. *J. Biol. Chem.* 282, 9458–9468.
- Sanchez, Y., Wong, C., Thoma, R.S., Richman, R., Wu, Z., Piwnicka-Worms, H., and Elledge, S.J. (1997). Conservation of the Chk1 checkpoint pathway in mammals: linkage of DNA damage to Cdk regulation through Cdc25. *Science* 277, 1497–1501.
- Mailand, N., Falck, J., Lukas, C., Syljuåsen, R.G., Welcker, M., Bartek, J., and Lukas, J. (2000). Rapid destruction of human Cdc25A in response to DNA damage. *Science* 288, 1425–1429.
- Peng, C.Y., Graves, P.R., Thoma, R.S., Wu, Z., Shaw, A.S., and Piwnicka-Worms, H. (1997). Mitotic and G2 checkpoint control: regulation of 14-3-3 protein binding by phosphorylation of Cdc25C on serine-216. *Science* 277, 1501–1505.
- Lee, J., Kumagai, A., and Dunphy, W.G. (2001). Positive regulation of Wee1 by Chk1 and 14-3-3 proteins. *Mol. Biol. Cell* 12, 551–563.
- Zou, L., and Elledge, S.J. (2003). Sensing DNA damage through ATRIP recognition of RPA-ssDNA complexes. *Science* 300, 1542–1548.
- Gong, Z., Kim, J.-E., Leung, C.C.Y., Glover, J.N.M., and Chen, J. (2010). BACH1/FANCD1 Acts with TopBP1 and Participates Early in DNA Replication Checkpoint Control. *Mol. Cell* 37, 438–446.
- Lee, W.T.C., Yin, Y., Morten, M.J., Tonzi, P., Gwo, P.P., Odermatt, D.C., Modesti, M., Cantor, S.B., Gari, K., Huang, T.T., and Rothenberg, E. (2021). Single-molecule imaging reveals replication fork coupled formation of G-quadruplex structures hinders local replication stress signaling. *Nat. Commun.* 12, 2525.
- Kumagai, A., Lee, J., Yoo, H.Y., and Dunphy, W.G. (2006). TopBP1 Activates the ATR-ATRIP Complex. *Cell* 124, 943–955.
- Duursma, A.M., Driscoll, R., Elias, J.E., and Cimprich, K.A. (2013). A role for the MRN complex in ATR activation via TOPBP1 recruitment. *Mol. Cell* 50, 116–122.
- Acevedo, J., Yan, S., and Michael, W.M. (2016). Direct Binding to Replication Protein A (RPA)-coated Single-stranded DNA Allows Recruitment of the ATR Activator TopBP1 to Sites of DNA Damage. *J. Biol. Chem.* 291, 13124–13131.
- Mordes, D.A., Glick, G.G., Zhao, R., and Cortez, D. (2008). TopBP1 activates ATR through ATRIP and a PIKK regulatory domain. *Genes Dev.* 22, 1478–1489.
- Lee, J., Kumagai, A., and Dunphy, W.G. (2007). The Rad9-Hus1-Rad1 checkpoint clamp regulates interaction of TopBP1 with ATR. *J. Biol. Chem.* 282, 28036–28044.
- Delacroix, S., Wagner, J.M., Kobayashi, M., Yamamoto, K.i., and Karnitz, L.M. (2007). The Rad9-Hus1-Rad1 (9-1-1) clamp activates checkpoint signaling via TopBP1. *Genes Dev.* 21, 1472–1477.
- Frattini, C., Promonet, A., Alghoul, E., Vidal-Eychenie, S., Lamarque, M., Blanchard, M.P., Urbach, S., Basbous, J., and Constantinou, A. (2021). TopBP1 assembles nuclear condensates to switch on ATR signaling. *Mol. Cell* 81, 1231–1245.e8.
- Dunphy, W.G. (2021). TopBP1 comes into focus. *Mol. Cell* 81, 1126–1127.
- Banani, S.F., Lee, H.O., Hyman, A.A., and Rosen, M.K. (2017). Biomolecular condensates: organizers of cellular biochemistry. *Nat. Rev. Mol. Cell Biol.* 18, 285–298.
- Mathieu, C., Pappu, R.V., and Taylor, J.P. (2020). Beyond aggregation: Pathological phase transitions in neurodegenerative disease. *Science* 370, 56–60.
- Putnam, A., Thomas, L., and Seydoux, G. (2023). RNA granules: functional compartments or incidental condensates? *Genes Dev.* 37, 354–376.
- Lyon, A.S., Peebles, W.B., and Rosen, M.K. (2021). A framework for understanding the functions of biomolecular condensates across scales. *Nat. Rev. Mol. Cell Biol.* 22, 215–235.
- Shin, Y., and Brangwynne, C.P. (2017). Liquid phase condensation in cell physiology and disease. *Science* 357, eaaf4382.
- Alberti, S., Gladfelter, A., and Mittag, T. (2019). Considerations and Challenges in Studying Liquid-Liquid Phase Separation and Biomolecular Condensates. *Cell* 176, 419–434.

31. Alberti, S., and Hyman, A.A. (2021). Biomolecular condensates at the nexus of cellular stress, protein aggregation disease and ageing. *Nat. Rev. Mol. Cell Biol.* *22*, 196–213.
32. Musacchio, A. (2022). On the role of phase separation in the biogenesis of membraneless compartments. *EMBO J.* *41*, e109952. <https://doi.org/10.15252/embj.2021109952>.
33. Mittag, T., and Pappu, R.V. (2022). A conceptual framework for understanding phase separation and addressing open questions and challenges. *Mol. Cell* *82*, 2201–2214.
34. Pappu, R.V., Cohen, S.R., Dar, F., Farag, M., and Kar, M. (2023). Phase Transitions of Associative Biomacromolecules. *Chem. Rev.* *123*, 8945–8987. <https://doi.org/10.1021/acs.chemrev.2c00814>.
35. Nott, T.J., Petsalaki, E., Farber, P., Jervis, D., Fussner, E., Plochowitz, A., Craggs, T.D., Bazett-Jones, D.P., Pawson, T., Forman-Kay, J.D., and Baldwin, A.J. (2015). Phase transition of a disordered nuage protein generates environmentally responsive membraneless organelles. *Mol. Cell* *57*, 936–947.
36. Hyman, A.A., and Simons, K. (2012). Cell biology. Beyond oil and water-phase transitions in cells. *Science* *337*, 1047–1049.
37. Wang, J., Choi, J.M., Holehouse, A.S., Lee, H.O., Zhang, X., Jahnel, M., Maharana, S., Lemaître, R., Pozniakovskiy, A., Drechsel, D., et al. (2018). A Molecular Grammar Governing the Driving Forces for Phase Separation of Prion-like RNA Binding Proteins. *Cell* *174*, 688–699.e16.
38. Yamazaki, H., Takagi, M., Kosako, H., Hirano, T., and Yoshimura, S.H. (2022). Cell cycle-specific phase separation regulated by protein charge blockiness. *Nat. Cell Biol.* *24*, 625–632.
39. Valverde, J.M., Dubra, G., Phillips, M., Haider, A., Elena-Real, C., Fournet, A., Alghoul, E., Chahar, D., Andrés-Sánchez, N., Paloni, M., et al. (2023). A cyclin-dependent kinase-mediated phosphorylation switch of disordered protein condensation. *Nat. Commun.* *14*, 6316.
40. Thada, V., and Cortez, D. (2019). Common motifs in ETAA1 and TOPBP1 required for ATR kinase activation. *J. Biol. Chem.* *294*, 8395–8402.
41. Smits, V.A.J., Reaper, P.M., and Jackson, S.P. (2006). Rapid PIKK-dependent release of Chk1 from chromatin promotes the DNA-damage checkpoint response. *Curr. Biol.* *16*, 150–159.
42. Liu, S., Bekker-Jensen, S., Mailand, N., Lukas, C., Bartek, J., and Lukas, J. (2006). Claspin operates downstream of TopBP1 to direct ATR signaling towards Chk1 activation. *Mol. Cell Biol.* *26*, 6056–6064.
43. Furnari, B., Rhind, N., and Russell, P. (1997). Cdc25 mitotic inducer targeted by chk1 DNA damage checkpoint kinase. *Science* *277*, 1495–1497.
44. Boos, D., Sanchez-Pulido, L., Rappas, M., Pearl, L.H., Oliver, A.W., Ponting, C.P., and Diffley, J.F.X. (2011). Regulation of DNA Replication through Sld3-Dpb11 Interaction Is Conserved from Yeast to Humans. *Curr. Biol.* *21*, 1152–1157.
45. Kumagai, A., Shevchenko, A., Shevchenko, A., and Dunphy, W.G. (2010). Treslin Collaborates with TopBP1 in Triggering the Initiation of DNA Replication. *Cell* *140*, 349–359.
46. Tercero, J.A., Longhese, M.P., and Diffley, J.F.X. (2003). A central role for DNA replication forks in checkpoint activation and response. *Mol. Cell* *11*, 1323–1336.
47. O'Neill, B.M., Szyjka, S.J., Lis, E.T., Bailey, A.O., Yates, J.R., 3rd, Aparicio, O.M., and Romesberg, F.E. (2007). Pph3-Psy2 is a phosphatase complex required for Rad53 dephosphorylation and replication fork restart during recovery from DNA damage. *Proc. Natl. Acad. Sci. USA* *104*, 9290–9295.
48. Szyjka, S.J., Aparicio, J.G., Viggiani, C.J., Knott, S., Xu, W., Tavaré, S., and Aparicio, O.M. (2008). Rad53 regulates replication fork restart after DNA damage in *Saccharomyces cerevisiae*. *Genes Dev.* *22*, 1906–1920.
49. Willis, N., and Rhind, N. (2009). Regulation of DNA replication by the S-phase DNA damage checkpoint. *Cell Div.* *4*, 13.
50. Bacal, J., Moriel-Carretero, M., Pardo, B., Barthe, A., Sharma, S., Chabes, A., Lengronne, A., and Pasero, P. (2018). Mrc1 and Rad9 cooperate to regulate initiation and elongation of DNA replication in response to DNA damage. *EMBO J.* *37*, e99319.
51. McClure, A.W., and Diffley, J.F. (2021). Rad53 checkpoint kinase regulation of DNA replication fork rate via Mrc1 phosphorylation. *Elife* *10*, e69726.
52. Seiler, J.A., Conti, C., Syed, A., Aladjem, M.I., and Pommier, Y. (2007). The intra-S-phase checkpoint affects both DNA replication initiation and elongation: single-cell and -DNA fiber analyses. *Mol. Cell Biol.* *27*, 5806–5818.
53. Alghoul, E., Paloni, M., Takedachi, A., Urbach, S., Barducci, A., Gaillard, P.H., Basbous, J., and Constantinou, A. (2023). Compartmentalization of the SUMO/RNF4 pathway by SLX4 drives DNA repair. *Mol. Cell* *83*, 1640–1658.e9. <https://doi.org/10.1016/j.molcel.2023.03.021>.
54. Kilic, S., Lezaja, A., Gatti, M., Bianco, E., Michelena, J., Imhof, R., and Altmeyer, M. (2019). Phase separation of 53BP1 determines liquid-like behavior of DNA repair compartments. *EMBO J.* *38*, e101379.
55. Alghoul, E., Basbous, J., and Constantinou, A. (2021). An optogenetic proximity labeling approach to probe the composition of inducible biomolecular condensates in cultured cells. *STAR Protoc.* *2*, 100677.
56. Leung, C.C.Y., Gong, Z., Chen, J., and Glover, J.N.M. (2011). Molecular basis of BACH1/FANCD1 recognition by TopBP1 in DNA replication checkpoint control. *J. Biol. Chem.* *286*, 4292–4301.
57. Cantor, S.B., Bell, D.W., Ganesan, S., Kass, E.M., Drapkin, R., Grossman, S., Wahrer, D.C., Sgroi, D.C., Lane, W.S., Haber, D.A., and Livingston, D.M. (2001). BACH1, a novel helicase-like protein, interacts directly with BRCA1 and contributes to its DNA repair function. *Cell* *105*, 149–160.
58. Harms, M.J., Schlessman, J.L., Sue, G.R., and García-Moreno, E.,B. (2011). Arginine residues at internal positions in a protein are always charged. *Proc. Natl. Acad. Sci. USA* *108*, 18954–18959.
59. Nam, E.A., Zhao, R., Glick, G.G., Bansbach, C.E., Friedman, D.B., and Cortez, D. (2011). Thr-1989 phosphorylation is a marker of active ataxia telangiectasia-mutated and Rad3-related (ATR) kinase. *J. Biol. Chem.* *286*, 28707–28714.
60. Liu, S., Shiotani, B., Lahiri, M., Maréchal, A., Tse, A., Leung, C.C.Y., Glover, J.N.M., Yang, X.H., and Zou, L. (2011). ATR autophosphorylation as a molecular switch for checkpoint activation. *Mol. Cell* *43*, 192–202.
61. Li, P., Goto, H., Kasahara, K., Matsuyama, M., Wang, Z., Yatabe, Y., Kiyono, T., and Inagaki, M. (2012). P90 RSK arranges Chk1 in the nucleus for monitoring of genomic integrity during cell proliferation. *MBoC* *23*, 1582–1592.
62. Peddibhotla, S., Wei, Z., Papineni, R., Lam, M.H., Rosen, J.M., and Zhang, P. (2011). The DNA damage effector Chk1 kinase regulates Cdc14B nuclear shuttling during cell cycle progression. *Cell Cycle* *10*, 671–679.
63. Zhang, Q., Kerzhnerman, M.A., García-Vázquez, N., and Rona, G. (2023). Visualizing Single-Stranded DNA Foci in the G1 Phase of the Cell Cycle. *JoVE* *65926*. <https://doi.org/10.3791/65926>.
64. Lossaint, G., Larroque, M., Ribeyre, C., Bec, N., Larroque, C., Décaillot, C., Gari, K., and Constantinou, A. (2013). FANCD2 Binds MCM Proteins and Controls Replisome Function upon Activation of S Phase Checkpoint Signaling. *Mol. Cell* *51*, 678–690.
65. McSwiggen, D.T., Mir, M., Darzacq, X., and Tjian, R. (2019). Evaluating phase separation in live cells: diagnosis, caveats, and functional consequences. *Genes Dev.* *33*, 1619–1634.
66. Muzzopappa, F., Hummert, J., Anfossi, M., Tashev, S.A., Herten, D.P., and Erdel, F. (2022). Detecting and quantifying liquid-liquid phase separation in living cells by model-free calibrated half-bleaching. *Nat. Commun.* *13*, 7787.
67. Spegg, V., Panagopoulos, A., Stout, M., Krishnan, A., Reginato, G., Imhof, R., Roschitzki, B., Cejka, P., and Altmeyer, M. (2023). Phase separation properties of RPA combine high-affinity ssDNA binding with dynamic condensate functions at telomeres. *Nat. Struct. Mol. Biol.* *30*, 451–462.
68. Ellis, R.J. (2001). Macromolecular crowding: obvious but underappreciated. *Trends Biochem. Sci.* *26*, 597–604.

69. Alghoul, E., Basbous, J., and Constantinou, A. (2023). Compartmentalization of the DNA damage response: Mechanisms and functions. *DNA Repair* 128, 103524.
70. Piradashvili, K., Alexandrino, E.M., Wurm, F.R., and Landfester, K. (2016). Reactions and Polymerizations at the Liquid-Liquid Interface. *Chem. Rev.* 116, 2141–2169.
71. Dai, Y., Chamberlayne, C.F., Messina, M.S., Chang, C.J., Zare, R.N., You, L., and Chilkoti, A. (2023). Interface of biomolecular condensates modulates redox reactions. *Chem* 9, 1594–1609.
72. Yan, Z., Ge, X., Wang, J., Xu, F., Li, M., Liu, X., Yu, X., and Wu, C. (2022). The impact of TOPBP1 mutations in human cancers on the DNA damage response. *GENOME INSTAB. DIS.* 3, 144–162.
73. Egger, T., Bordignon, B., and Coquelle, A. (2022). A clinically relevant heterozygous ATR mutation sensitizes colorectal cancer cells to replication stress. *Sci. Rep.* 12, 5422.
74. Goedhart, J. (2021). SuperPlotsOfData—a web app for the transparent display and quantitative comparison of continuous data from different conditions. *MBoC* 32, 470–474.

## STAR★METHODS

### KEY RESOURCES TABLE

REAGENT or RESOURCE	SOURCE	IDENTIFIER
<b>Antibodies</b>		
TopBP1	Santa Cruz Biotechnology	Cat# sc-271043; RRID:AB_10610636
BRCA1(C-20)	Santa Cruz Biotechnology	Cat# sc-642; RRID:AB_630944
FANCF	Novus Biologicals	NBP1-31883; RRID:AB_2066306
Phospho-Chk1 (S345)	Cell Signaling Technology	Cat# 2341; RRID:AB_330023
BrdU/IdU	BD Biosciences	Cat# 347580; RRID:AB_10015219
Tubulin (B-5-1-2)	Sigma-Aldrich	Cat# T5168; RRID:AB_477579
Alexa Fluor 546 goat anti-mouse IgG	Molecular Probes	Cat# A-11030; RRID:AB_144695
Alexa Fluor 488 goat anti-rabbit IgG	Molecular Probes	Cat# A-21141; RRID:AB_141626
Anti-rabbit IgG, HRP linked	Cell Signaling Technology	Cat# 7074; RRID:AB_2099233
Anti-mouse IgG, HRP linked	Cell Signaling Technology	Cat# 7076; RRID:AB_330924
Anti-Rabbit-IgG - Atto 647N	Sigma-Aldrich	Cat# 40839; RRID:AB_1137669
STAR ORANGE, goat anti-mouse IgG, 500 $\mu$ L (1 mg/mL)	Abberior	Cat# STORANGE-1001; RRID:AB_2847853
Replication Protein A 2 (RPA2)	Abcam	Cat# ab2175; RRID:AB_302873
Phospho-ATR (T1989)	GeneTex	Cat# GTX128145; RRID:AB_2687562
ATR	Cell Signaling Technology	Cat# 2790; RRID:AB_2227860
CldU	Bio-Rad	Cat# OBT-0030, RRID:AB_2314029
Phospho-Histone H2A.X (S139)	Cell Signaling Technology	Cat# 9718; RRID:AB_2118009
Histone H2A.X	Cell Signaling Technology	Cat# 2595; RRID:AB_10694556
Vinculin	Sigma-Aldrich	Cat# V9131; RRID:AB_477629
Phospho-TopBP1 (S1138)	Affinity Biosciences	Cat# AF3564, RRID:AB_2846878
Phospho-RPA2 (S33)	Bethyl	Cat# A300-246A, RRID:AB_2180847
Chk1 (G-4)	Santa Cruz Biotechnology	Cat# sc-8408; RRID:AB_627257
Claspin	Bethyl	Cat# A300-266A, RRID:AB_155895
Alexa Fluor 568 goat anti-mouse IgG	Thermo Fisher Scientific	Cat# A-11004, RRID:AB_2534072
<b>Bacterial and virus strains</b>		
5-alpha Competent <i>E. coli</i> (High Efficiency)	NEB	Cat# C2987
<b>Chemicals, peptides, and recombinant proteins</b>		
Biotin	Sigma-Aldrich	Cat# B4501; CAS: 58-85-5
Doxycycline	Clontech	Cat# 631311; CAS: 10592-13-9
Blasticidin	InvivoGen	Cat# ant-bl
Hygromycin	Sigma-Aldrich	Cat# H3274; CAS: 31282-04-9
Ampicilin	Sigma-Aldrich	Cat# A9518; CAS: 69-52-3
cOmplete, EDTA free	Roche	Cat# 4693159001
Halt phosphatase inhibitor cocktail	ThermoFisher Scientific	Cat# 78427
Benzonase Nuclease	Sigma-Aldrich	Cat# E1014; CAS: 9025-65-4
Streptavidin-Agarose	Sigma-Aldrich	Cat# S1638; MDL: MCFD00082035
Dulbecco's Modified Eagle's Medium - high glucose	Sigma-Aldrich	Cat# D5796
BioWest - Fetal Bovine Serum	Eurobio Scientific	Cat# S1810
Glycerol $\geq$ 99.5%	VWR Chemicals	Cat# 24388.295; CAS: 56-81-5
Bromophenol Blue	Ethylenediaminetetraacetic acid	Cat# B0126; CAS: 115-39-9
Ethylenediaminetetraacetic acid	Ethylenediaminetetraacetic acid	Cat# EDS; CAS: 60-00-4

(Continued on next page)

**Continued**

REAGENT or RESOURCE	SOURCE	IDENTIFIER
HEPES	Sigma-Aldrich	Cat# H3375; CAS: 7365-45-9
Sodium Chloride	VWR Chemicals	Cat# 27810-295; CAS: 7647-14-5
Triton X-100	Sigma-Aldrich	Cat# T8787; CAS: 9002-93-1
Tergitol Solution type NP-40	Sigma-Aldrich	Cat# NP40S; MDL: MFCD01779855
Sodium dodecyl sulfate 20%	BIOSOLVE	Cat# 198123; CAS: 151-21-3
Tris base	Euromedex	Cat# 200923-A; CAS: 77-86-1
Dulbecco's Phosphate Buffered Saline	Sigma-Aldrich	Cat# D8537; MDL: MFCD00131855
Water	Sigma-Aldrich	Cat# W3500; CAS: 7732-18-5
Bovine Serum Albumin (BSA), Fraction V	Euromedex	Cat# 04-100-812-C CAS: 90604-29-8 9048-46-8
2-Mercaptoethanol	Sigma-Aldrich	Cat# M3148; CAS: 60-24-2
5-Iodo-2'-deoxyuridine	Sigma-Aldrich	Cat# I7125; CAS: 54-42-2
5-Chloro-2'-deoxyuridine	Sigma-Aldrich	Cat# C6891; CAS: 50-90-8
DMSO	Sigma-Aldrich	Cat# 276855; CAS: 67-68-5
Formaldehyde 32% Solution	Euromedex	Cat# EM-15714
TWEEN® 20	Sigma-Aldrich	Cat# P9416; CAS: 9005-64-5
(S)-(+)-Camptothecin	Sigma-Aldrich	Cat# C9911; CAS: 7689-03-4
Janelia Fluor JFX554 halo tag ligand	Promega	Cat# CS315101
Janelia Fluor JF549 halo tag ligand	Promega	GA1120
Hydrochloric acid 37%	VWR chemicals	Cat# 707652; CAS: 7647-01-0

**Critical commercial assays**

Clarity western ECL substrate	Bio-Rad	Cat# 170-5061
Clarity max western ECL substrate	Bio-Rad	Cat# 1705062
Criterion TGX stain free gel 4–15%	Bio-Rad	Cat# 5678084
Trans-Blot Turbo Transfer Pack 0.2µm	Bio-Rad	Cat# 1704159
Nitrocellulose Midi, 10 pack		
Color Prestained Protein Standard, Broad Range	BioLabs	Cat# P7712S
Lipofectamine 2000	ThermoFisher Scientific	Cat# 11668-019
Quick change multi site directed	Agilent technologies	Cat# 200515-5
Prolong gold antifade	ThermoFisher Scientific	Cat# P10144
Pierce™ BCA Protein Assay Kit	ThermoFisher Scientific	Cat# 23227

**Deposited data**

Raw data	This paper	Mendeley data set <a href="https://doi.org/10.17632/zdb9ccrpm6.1">https://doi.org/10.17632/zdb9ccrpm6.1</a>
----------	------------	---

**Experimental models: cell lines**

Flp-In™ T-REx™ 293	Invitrogen	Cat# R78007; RRID:CVCL_U427
HEK293T	Sigma-Aldrich	Cat# 12022001; RRID:CVCL_0063
WT Human Primary Fibroblasts	Kind gift from Gérald Lossaint	N/A
E6/E7 Human Primary Fibroblasts	Kind gift from Gérald Lossaint	N/A
CL-HJL-0105-A KI HEK293T Halo-TopBP1	Biocytogen	N/A

**Oligonucleotides**

See <a href="#">Table S1</a> for the full list of oligonucleotides used in this study	This paper	N/A
---	------------	-----

**Recombinant DNA**

pCDNA5_FRT_TO_TurboID-mCherry-Cry2 (opto module)	Addgene	Cat# 166504; <a href="http://n2t.net/addgene:166504">http://n2t.net/addgene:166504</a> ; RRID:Addgene_166504
pOG44 Flp-Recombinase Expression Vector	ThermoFisher Scientific	Cat# V600520

(Continued on next page)

**Continued**

REAGENT or RESOURCE	SOURCE	IDENTIFIER
pCRISPaint-HaloTag-PuroR	Addgene	Cat# 80960; <a href="http://n2t.net/addgene:80960">http://n2t.net/addgene:80960</a> ; RRID:Addgene_80960
pCDNA5_FRT-TO_TurboID-TopBP1WT-mCherry-Cry2	Frattini et al., molcel (2021) <sup>23</sup>	N/A
pCDNA5_FRT-TO_TurboID-TopBP1S1273A-mCherry-Cry2	This paper	N/A
pCDNA5_FRT-TO_TurboID-TopBP1R1280Q-mCherry-Cry2	This paper	N/A
pCDNA5_FRT-TO_TurboID-TopBP1R1314Q-mCherry-Cry2	This paper	N/A
pCDNA5_FRT-TO_TurboID-TopBP1M1-mCherry-Cry2	This paper	N/A
pCDNA5_FRT-TO_TurboID-TopBP1M2-mCherry-Cry2	This paper	N/A
pCDNA5_FRT-TO_TurboID-TopBP1M3-mCherry-Cry2	This paper	N/A
pCDNA5_FRT-TO_TurboID-TopBP1M4-mCherry-Cry2	This paper	N/A
pCDNA5_FRT-TO_TurboID-TopBP1M5-mCherry-Cry2	This paper	N/A
pCDNA5_FRT-TO_TurboID-TopBP1M3R-mCherry-Cry2	This paper	N/A

**Software and algorithms**

OMERO	OME Remote Objects software	RRID:SCR_002629
Image Lab™ Software (Version 5.2.1)	Bio-Rad	RRID:SCR_014210
Biorender Software	Science Suite Inc.	RRID:SCR_018361
Prism 8 (Version 8.4.2)	Graphpad Software	RRID:SCR_002798
FIJI	Open source	RRID:SCR_002285
Kaluza Aquisition Software	Beckman Coulter	RRID:SCR_016182
Kaluza Analysis Software	Beckman Coulter	RRID:SCR_016182
Cell Profiler 4.2.1	CellProfiler Image Analysis Software	RRID:SCR_007358
ZEN Blue	Zeiss	RRID:SCR_013672

**Other**

CO <sub>2</sub> Incubator C150	Binder	Cat# 9040-0078
Sonicator, VibraCell- 72405	BioBlock scientific	N/A
Centrifuge Hettich Mikro 200	Grosseron	N/A
Criterion™ Cell	Bio-Rad	Cat# 1656001
PowerPac™ HC High-Current Power Supply	Bio-Rad	Cat# 1645052
Trans-Blot Turbo Transfer System	Bio-Rad	Cat# 1704150
Gallios Flow Cytometer	Beckman Coulter Gallios Flow Cytometer	RRID:SCR_019639
Zen Axio Imager 2	Zeiss	RRID:SCR_018876

**RESOURCE AVAILABILITY**

**Lead contact**

Further information and requests for resources and reagents should be directed to the lead contact, Jihane Basbous, correspondence: [jihane.basbous@igh.cnrs.fr](mailto:jihane.basbous@igh.cnrs.fr).

**Materials availability**

All unique reagents generated from this study are available without restriction upon request to the **lead contact**, Jihane Basbous, correspondence: [jihane.basbous@igh.cnrs.fr](mailto:jihane.basbous@igh.cnrs.fr).

### Data and code availability

- Data have been deposited at Mendeley and are publicly available as of the date of publication. <https://doi.org/10.17632/zdb9ccrpm6.1> and see [key resources table](#).
- This paper does not report original code.
- Any additional information required to re-analyse the data reported in this paper is available from the [lead contact](#) upon request.

## EXPERIMENTAL MODEL AND STUDY PARTICIPANT DETAILS

### Human cell lines

Fip-In T-REx 293 cells were obtained from Thermo Fisher and cultured in DMEM-GlutaMax medium supplemented with 10% FBS. Cells were maintained at 37°C, 5% CO<sub>2</sub> in saturated humidity.

For the generation of WT and mutant TopBP1<sup>opto</sup> stable cell lines, 1.2 × 10<sup>6</sup> cells were transfected with TopBP1<sup>opto</sup> constructs in 6 well plates following the instructions of the manufacturer. 0.5 μg of the TopBP1<sup>opto</sup> plasmid were co-transfected along with 3.5 μg of pOG44 in Opti-MEM using Lipofectamine 2000 (Thermo Fisher), following the manufacturer's instructions. The medium was changed the following day and cells were split in T<sub>75</sub> flasks at day 2. Selection with antibiotics was performed at day 3 (5 μg/mL Blasticidin and 50 μg/mL Hygromycin). Medium was changed every 2–3 days until day 12–15. At this point, cells were dissociated, amplified and frozen. For the experiments, cells were seeded in selection-free medium, containing (or not) 2 μg/mL of doxycycline (referred as “DOX” in figures) to induce the expression of the Opto-TopBP1 transgenes. Typically, 1.2 × 10<sup>6</sup> cells were seeded per well in 6-well plates the day prior to the experiments.

TopBP1<sup>Halo/Halo</sup> cell line: HEK293 cells stably expressing endogenous TopBP1 tagged on its C terminus with HaloTag on both alleles were generated using a CRISPR/Cas9 based Biocytogen Extreme Genome Editing System (EGE) and cultured in DMEM-GlutaMax medium supplemented with 10% FBS. Cells were maintained at 37°C, 5% CO<sub>2</sub> in saturated humidity. To detect TopBP1<sup>Halo</sup> (Figures 4 and S5A), cells were incubated with 200 nM of Janelia Fluor HaloTag JFX554 or JF646 (as described) for 15 min at 37°C prior to cell fixation.

Human Dermal Fibroblasts (HDF) expressing or not E6 and E7 proteins from HPV-16 (namely WT vs. E6/E7) were previously described<sup>64</sup> and cultured in DMEM-GlutaMax medium supplemented with 10% FBS. Cells were maintained at 37°C, 5% CO<sub>2</sub> in saturated humidity.

## METHOD DETAILS

### Generation of mutant Opto-TopBP1 plasmids

The plasmid encoding WT TopBP1<sup>opto</sup> was edited using the QuikChange Multi Site-Directed Mutagenesis Kit according to the manufacturer's instructions. Mutagenic primer sequences used to generate the ADD mutants were described in [STAR Methods](#). Briefly, a PCR was performed using 100 ng of mutagenic primers and 100 ng template DNA (WT TopBP1<sup>opto</sup> plasmid), according to Agilent's instructions. The PCR products were then digested with DpnI and used to transform NEB5-Alpha competent *E. coli* according to the manufacturer's instructions. Isolated clones that grew under Ampicillin selection were randomly picked and amplified overnight at 37°C under agitation. Midi-preps were conducted to isolate the mutated plasmids. Mutations were verified by a full sequencing of the purified plasmids. Validated constructs were then transfected in Fip-In T-REx 293 (see above, [human cell lines](#)).

### Treatments

For the light induction of TopBP1<sup>opto</sup> condensation, cells were exposed to pulses of 488 nm blue light for 3 min (cycles of 4 s “ON” and 10 s “OFF”) as described,<sup>23</sup> unless stated otherwise. For camptothecin (CPT) treatment, cells were treated with 1 μM of CPT for the indicated duration (1h).

### Antibodies

See [STAR Methods](#) table.

### Immunofluorescence

1.2 × 10<sup>6</sup> cells were seeded in 6-well plates with or without DOX, on 1.5H high precision glass coverslips pre-coated with poly-D-lysine according to the manufacturer's instruction and let overnight to attach and start proliferating.

If pre-extraction was required (chromatin-bound RPA2, Figures 4, S1C, and S4A), cells were immediately pre-extracted in ice-cold PBS containing 0.2% Triton X-100 for 3 min on ice. Cells were washed in PBS and fixed in PBS containing 4% paraformaldehyde (PFA) for 15 min at room temperature (RT) before being washed twice in PBS. Otherwise, cells were immediately fixed in PBS containing 4% paraformaldehyde (PFA) for 15 min at room temperature (RT), washed twice in PBS and permeabilized in PBS with 0.2% Triton X-100 for 15 min at RT. For both conditions, the following steps are identical. Cells were saturated using 1X Perm/Wash buffer for 1h at RT. Coverslips were then transferred onto Parafilm and placed in humid chambers, and 100 μL of 1X Perm/Wash containing the appropriate dilution of primary antibodies were gently pipetted onto them. Incubation with the primary antibodies was performed overnight (O/N) at 4°C in the humid chambers. Coverslips were then washed 3 × 5 min in 1X Perm/Wash buffer at RT. Next, 100 μL of

1X Perm/Wash containing 1/250 of secondary antibodies were gently pipetted on the coverslips. Secondary antibodies were incubated for 1h at RT, in humid chambers (in the dark). Coverslips were then washed 3 × 5 min in 1X Perm/Wash buffer at RT. 100 μL of PBS containing 5 μg/mL Hoechst 33342 were pipetted onto the coverslips to counterstain the DNA for (10 min at RT). Coverslips were then washed twice in PBS and once in dH<sub>2</sub>O before being mounted onto SuperFrost microscopy slides using Prolong Gold Anti-Fade. Preparations were allowed to rest at room temperature for at least 24 h before imaging on a Zeiss Axio Imager microscope equipped with the ApoTome.2 technology, with an ×63 immersion Plan Achromatic objective (NA 1.46 oil). At least 10 fields were randomly imaged per sample using the DNA (Hoechst) channel. Image processing and quantification were later performed using CellProfiler 4.2.1 software (see below). All micrographs presented throughout the manuscript were displayed using OME Remote Objects (OMERO) software.

### CellProfiler 4.2.1 pipelines

The pipelines are available in the dedicated Mendeley data set (see [STAR Methods](#)). Briefly, metadata were extracted from Apotome RAW converted.czi files (Zeiss, Zen Blue 2.3). Channels (Hoechst C = 0, Alexa 488 C = 1, mCherry C = 2, Alexa 647 C = 3) were identified. Automated nuclear detection and segmentation was performed using the IdentifyPrimaryObject function with the Otsu Two classes thresholding method. Nuclear foci of each target protein were detected in a similar way, after an enhancement step (EnhanceOrSuppressFeatures, speckles, size = 10), with the manual thresholding method, before finally being related to their parent nucleus (RelatedObject function). Colocalizing objects were identified as the overlapping parts of different colored foci and related to their parent nuclei using the same strategy. The percentage of colocalizing foci per nucleus was then calculated as the ratio of the number of colocalized foci versus total foci of a defined color in individual nuclei, i.e.,:

$$\% \text{ of ColorA+, ColorB foci} = \frac{(\text{Color A+B}) \text{ colocalized foci count}}{\text{Total color B foci count}}, \text{ per nucleus}$$

The MasksObjects function was applied to identify and quantify the area of colocalizing nuclear foci and the pixel-based coefficients, such as Pearson's correlation coefficient. These coefficients were calculated in individual TopBP1<sup>opto</sup> condensates. Quality controls of segmentation and focus identification were systematically performed using the GrayToColor and OverlayOutlines functions, reconstructing all analyzed images and outlying identified nuclei and foci of each color.

### STED microscopy

Flp-In 293 T-REx cells expressing TopBP1<sup>Halo</sup> were stained with 200 nM Janelia Fluor HaloTag JF554 for 15 min at 37°C. After 2 washes in pre-warmed medium, cells were fixed with 4% PFA and processed for immunostaining with the antibodies indicated, followed by Abberior conjugated secondary antibodies. STED imaging was performed using a quad scanning STED microscope (Expert Line, Abberior Instruments, Germany) equipped with a PlanSuperApo 100x/1.40 oil immersion objective (Olympus, Japan). JF646 and Abberior STAR Orange were imaged at 640 and 561 nm excitation respectively using a 755 nm depletion laser line. Detection was set to 650–750 nm and 570–630 nm, respectively. A dwell time of 10 ms was used. Images were collected in line accumulation mode (5 lines), the pinhole was set to 1.0 Airy units and a pixel size of 10 nm was used for all acquisitions.

### Western blotting

1.2 × 10<sup>6</sup> cells were seeded in 6-well plates. After 3 min of 488 nm light illumination (cycles of 4 s “ON” and 10 s “OFF”), cells were harvested by scraping in ice-cold PBS. For whole-cell extracts (WCE), proteins were extracted in 80 μL of lysis buffer (10 mM HEPES-KOH pH 7.5, 200 mM NaCl, 0.5% NP-40, 2 mM MgCl<sub>2</sub>, 1 mM DTT, 1 mM PMSF) completed with protease inhibitors, phosphatases inhibitors, and 1/1000 Benzamide nuclease. Cells were lysed for 15 min at RT under 1000 rpm agitation. Debris were pelleted at 13,000 g, for 20 min at 4°C. Total proteins were quantified using the BCA Protein Assay Kit. 5x Laemmli buffer containing β-mercaptoethanol was diluted into the samples to a final concentration of 1x. Samples were heated at 95°C for 5 min and equivalent amounts of protein were loaded onto Precast Protein Gels. Gels were run at 150 V in Tris/Glycine Running Buffer. Proteins were transferred onto 0.2 μM nitrocellulose membranes using a Trans-Blot Turbo Transfer System. Total proteins were stained with Ponceau S and membranes were saturated in TBS-0.1% Tween 20, 5% non-fat dry milk (1 h at RT). Target proteins were immunodetected ON at 4°C in TBS-0.1% Tween 20 and 5% (w/v) BSA under rolling motion. Membranes were rinsed 3 × 10 min in TBS-0.1% Tween 20 and incubated for 1 h at RT in a blocking buffer containing the secondary antibodies diluted 1/3000. Membranes were rinsed 3 × 10 min in TBS-0.1% Tween 20 and revealed using ECL Clarity or Clarity Max, using a ChemiDoc machine. Band intensities were quantified using ImageJ software.

### Turbid proximity assay

1.2 × 10<sup>6</sup> cells were seeded in 6 well plates and the expression of TopBP1<sup>opto</sup> constructs was induced by the addition of 2 μg/mL DOX, O/N. The next day, cells were exposed to 500 μM biotin and subjected to 10 min of 488 nm light illumination (cycles of 4 s “ON” and 10 s “OFF”). Cell lysis, protein extraction and biotin IP was performed as described.<sup>55</sup> Briefly, biotin labeled proximal Opto-TopBP1 proteins upon light-induced condensation were pulled down using streptavidin-coated beads and probed by immunoblotting (as described above) to detect proteins that are associated with TopBP1 condensates. 10% of input were loaded as controls.

## DNA fiber assay

$1.2 \times 10^6$  cells were seeded in 6-well plates. Cells were allowed to attach overnight and then sequentially pulsed with 20  $\mu$ M 5-iodo-2'-deoxyuridine (IdU) (20 min) and 200  $\mu$ M 5-chloro-2'-deoxyuridine (CldU) (20 min). Cells were subjected to  $2 \times 3$  min of 488 nm light induction during the second pulse at  $t = 0$  min and  $t = 10$  min. Cells were scraped in ice-cold PBS, washed and diluted in ice-cold PBS to  $0.5\text{--}1 \times 10^6$  cells/mL. 2  $\mu$ L of this cell suspension were pipetted on the edges of SuperFrost microscopy slides. After 2–5 min drying at RT, 7  $\mu$ L of DNA Spreading Buffer (200 mM Tris-HCl pH 7.5, 50 mM EDTA, 0.5% SDS) were mixed with the cell containing-drops. After 2–5 min drying at RT, slides were manually inclined ( $15^\circ\text{--}30^\circ$ ), spreading the DNA fibers, which were subsequently fixed in a 3:1 methanol/acetic acid solution (10 min at RT). Slides were washed in  $\text{dH}_2\text{O}$  and DNA was denatured in 2.5 M HCl for 1 h. Slides were washed and saturated in a blocking buffer (PBS containing 1% BSA and 0.1% Tween 20) for 1 h at RT. Slides were then incubated 1 h with a mix of anti-IdU and anti-CldU diluted 1/25 in PBS-0.1% Tween 20, at  $37^\circ\text{C}$  in humid chambers. Slides were washed  $5 \times 2$  min in PBS-0.1% Tween 20 and incubated for 30 min at  $37^\circ\text{C}$  with a mix of secondary antibodies diluted 1/50 in PBS-0.1% Tween 20. Slides were rinsed  $5 \times 2$  min in PBS-0.1% Tween 20, air dried and mounted under  $24 \times 50$  mm coverslips with 30  $\mu$ L of ProLong Gold Antifade mounting reagent. 20 representative pictures of each condition were taken on a Zeiss Axio Imager (63 $\times$  objective). 400 ( $2 \times 200$ ) ongoing replication signals (CldU+IdU+) were randomly measured using ImageJ. The CldU/IdU ratio of each replication tract was calculated and plotted. Non-parametric unpaired Mann-Whitney tests were used to determine the significance of the results (ns: non-significant; \*\*\*:  $p < 0.001$ ).

## Flow cytometry

Cell cycle profiling using BrdU/propidium iodide was performed as previously described.<sup>73</sup> Briefly, cells were pulsed with 10  $\mu$ M 5-bromo-2'-deoxyuridine (BrdU) for 15 min and fixed in ice-cold 70% ethanol. Cells were digested in 30 mM HCl, 0.5 mg/mL pepsin (20 min,  $37^\circ\text{C}$ ). DNA was denatured in 2 N HCl (20 min, RT) and BrdU was immunodetected using the anti-BrdU clone BU1/75 in PBS, 2% goat serum- 0.5% HEPES, 0.5% Tween 20 revealed by a goat anti-rat Alexa Fluor 488 secondary antibody. DNA was stained in PBS, 25  $\mu$ g/mL propidium iodide and cells were analyzed on a Gallios flow cytometer (Beckman Coulter). 20,000 cells were analyzed for each sample using the Kaluza dedicated software.

## QUANTIFICATION AND STATISTICAL ANALYSIS

When possible, all biological replicates were pooled and plotted using SuperPlotsOfData (<https://huygens.science.uva.nl/SuperPlotsOfData/>).<sup>74</sup> Data are plotted as means  $\pm$  standard deviation (SD). When helping the visualization, data distribution is displayed as a half-violin plot on the right-hand side of the dotplots. For the immunofluorescence and DNA fibers analyses, statistical significances were first calculated on whole groups using one-way ANOVA (data available in the dedicated Mendeley data set: <https://doi.org/10.17632/zdb9ccrpm6.1>) and confirmed using non-parametric unpaired Mann-Whitney tests on GraphPad Prism 5 (the non-normal distributions of foci scoring and colocalization data limiting the precision of ANOVA analyses). Welch's t-tests were applied to test the significance of western blot data. Fisher's exact tests were used to test the significance of the flow cytometry data. In all cases, significance thresholds were: ns: non-significant; \*:  $p < 0.05$ ; \*\*:  $p < 0.01$ ; \*\*\*:  $p < 0.001$ .

**Cell Reports, Volume 43**

**Supplemental information**

**Spatial organization and functions of Chk1  
activation by TopBP1 biomolecular condensates**

**Tom Egger, Laura Morano, Marie-Pierre Blanchard, Jihane Basbous, and Angelos Constantinou**

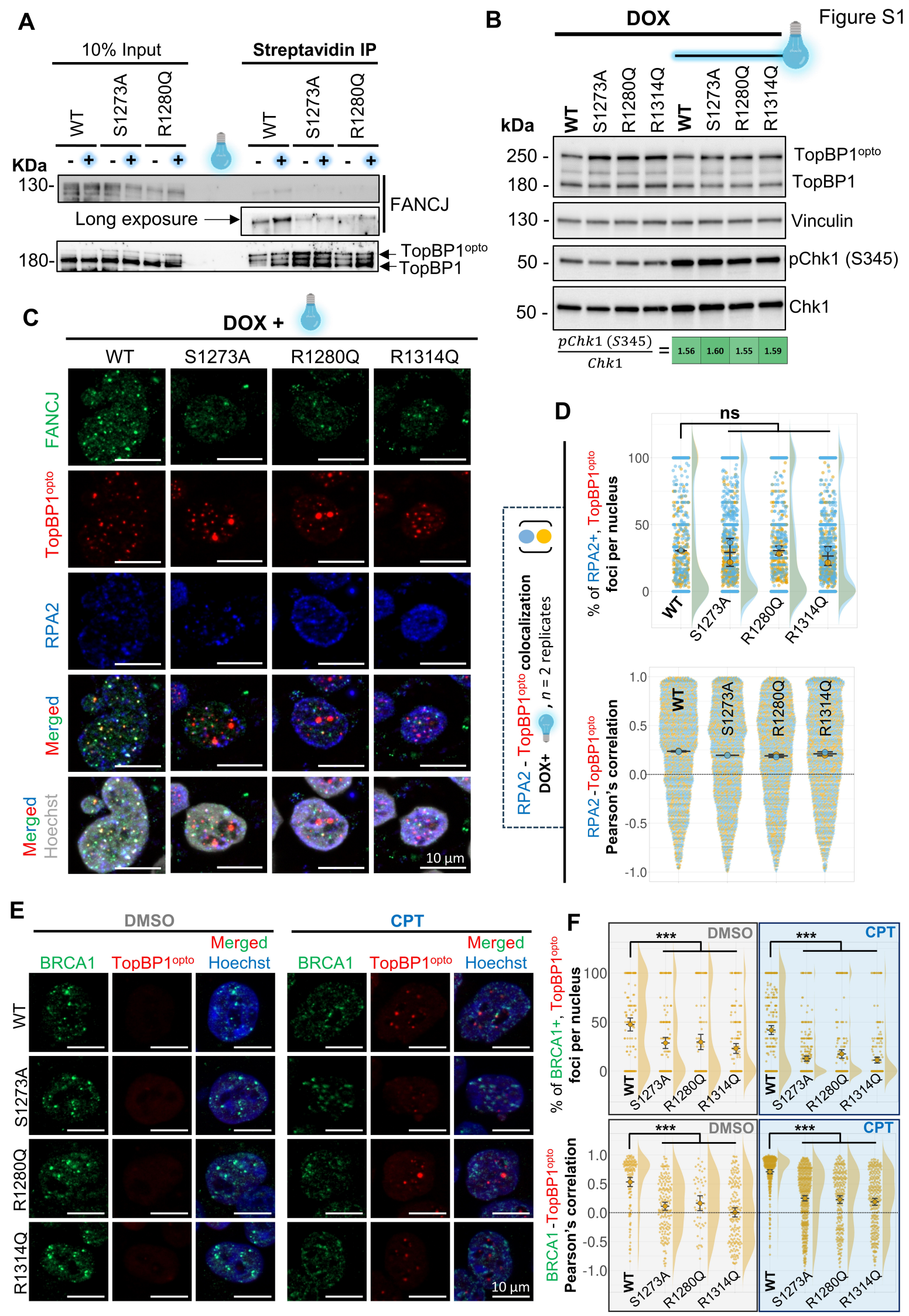


**Figure S1: TopBP1-FANCI interaction is dispensable for Chk1 activation but is necessary for BRCA1 localization at TopBP1 condensates upon DNA damage.**

(A) Representative immunoblots of TurboID proximity biotinylation of FANCI in cells expressing WT, S1273 and R1280 TopBP1<sup>opto</sup> constructs. Light bulbs: treatment by 3 min of 488 nm blue light.

(B) Immunoblotting of the proteins indicated from cells expressing WT or mutant TopBP1<sup>opto</sup> proteins, as indicated. Blue bulb: TopBP1<sup>opto</sup> condensates activated by light. Vinculin serves as a loading control. Lower panel: Normalized levels of pChk1 (S345) for the light-treated conditions.

(C) Representative micrographs of pre-extracted, light (488 nm)-induced (blue bulb) TopBP1<sup>opto</sup> condensates (red channel), immunodetected FANCI (green channel) and chromatin-bound RPA2 (blue channel) in cells expressing WT, S1273A, R1280Q or R1314Q TopBP1<sup>opto</sup> constructs. DNA is counterstained with Hoechst 33342 (artificial grey). Scale bars: 10  $\mu$ m.

(D) *Superplot* analysis of RPA2 colocalization with TopBP1<sup>opto</sup> condensates. Upper panel: object-based colocalization (percentage of RPA2 positive TopBP1<sup>opto</sup> foci per nucleus). Total number of analyzed nuclei (>1 TopBP1<sup>opto</sup> focus): WT: 1128, S1273A: 1446, R1280Q: 1239, R1314Q: 1658 (pool of 2 biological replicates). Data are plotted as means with SEMs and distribution is displayed as a half-violin plot on the right-hand side of the dotplots. Mann-Whitney tests were applied (ns: non-significant). Lower panel: pixel-based colocalization (Pearson's correlation coefficient in TopBP1<sup>opto</sup> foci). n=2 x 2000 foci were randomly selected in each condition (pool of 2 independent experiments). Data are plotted as means with SEMs.

(E) Representative micrographs of DMSO- or 1  $\mu$ M CPT-treated cells expressing WT, S1273A, R1280Q or R1314Q TopBP1<sup>opto</sup> constructs (red channel). BRCA1 is immunodetected in the green channel. DNA is counterstained with Hoechst 33342 (blue channel). Scale bars: 10  $\mu$ m.

(F) *Superplot* analysis of BRCA1 colocalization with TopBP1<sup>opto</sup> condensates. Upper panel: object-based colocalization (percentage of BRCA1 positive TopBP1<sup>opto</sup> foci per nucleus). Total number of analyzed nuclei (>1 TopBP1<sup>opto</sup> focus): WT: 142, S1273A: 162, R1280Q: 111, R1314Q: 171, WT+CPT: 274, S1273A+CPT: 342, R1280Q+CPT: 233, R1314Q+CPT: 285. Lower panel: pixel-based colocalization (Pearson's correlation coefficient in TopBP1<sup>opto</sup> foci). Up to 2000 foci were randomly selected in each condition. Data distribution is displayed as a half-violin plot on the right-hand side of the dotplots. Data are plotted as means with SEMs. Mann-Whitney tests were applied (\*\*\*: p<0.001).

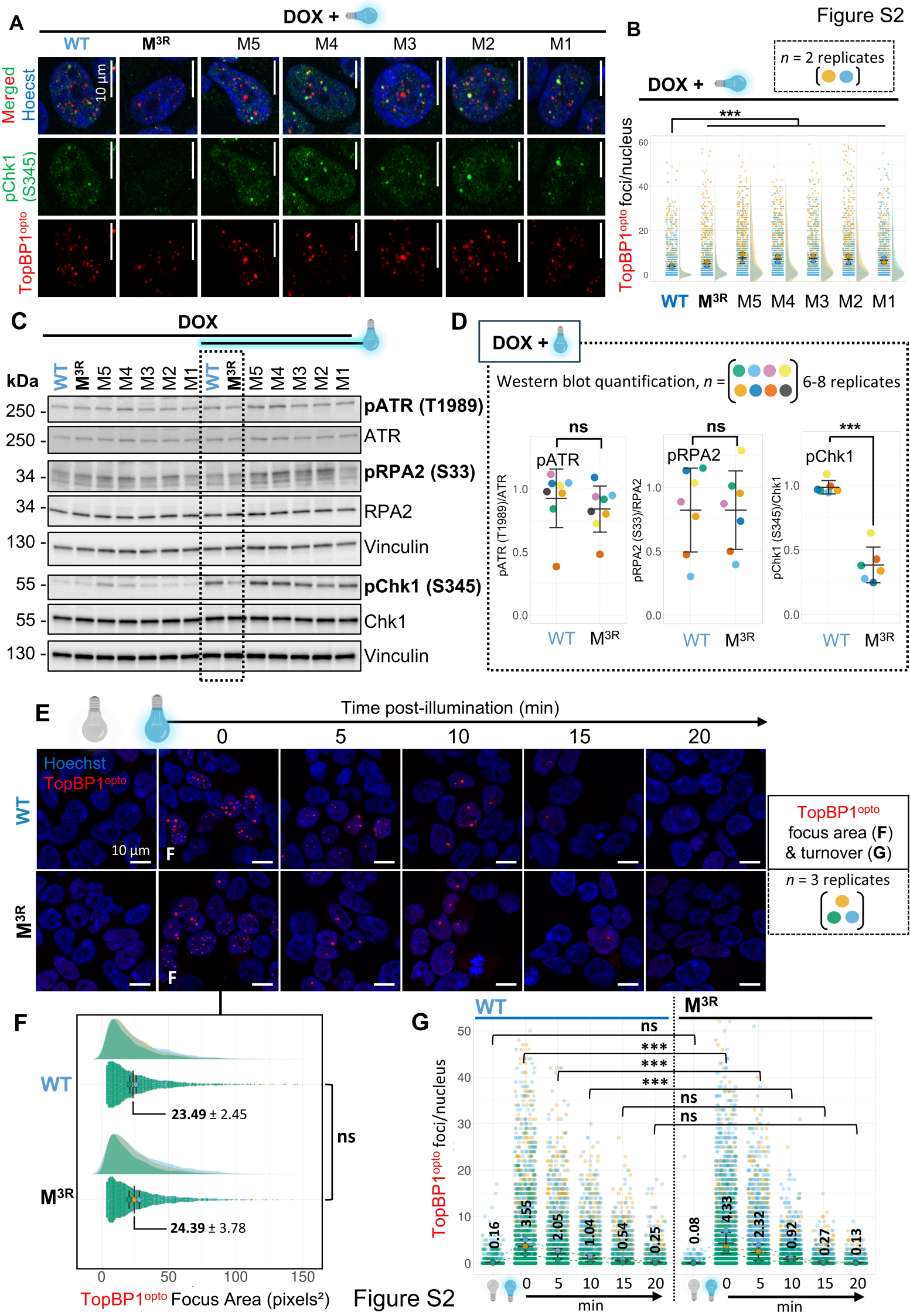


**Figure S2: M<sup>3R</sup> cells specifically lack Chk1 phosphorylation (S345) while retaining other markers of ATR activity.**

(A) Representative micrographs of light (488 nm)-induced (blue bulb) TopBP1<sup>opto</sup> condensates (red channel) and endogenous pChk1 (S345) (green channel) in cells expressing the indicated mutant TopBP1<sup>opto</sup> proteins (see Figure 2A). DNA is counterstained with Hoechst 33342 (blue channel). Scale bars: 10  $\mu$ m.

(B) *Superplot* analysis of the number of TopBP1<sup>opto</sup> condensates induced by optogenetic activation (488 nm blue light for 3 min) in cells expressing the indicated mutant TopBP1<sup>opto</sup> proteins (see Figure 2A). Data are plotted as means with SEMs. Number of analyzed nuclei per condition: WT: 1324, M3R: 1279, M5: 1188, M4: 1281, M3:1061, M2: 1252, M1: 1232. Mann-Whitney tests were applied (\*\*\*:  $p < 0.001$ ).

(C) Immunoblotting, with the antibodies indicated, of whole-cell extracts from cells expressing the indicated mutant TopBP1<sup>opto</sup> proteins. The blue bulb indicates that TopBP1 condensates were induced by optogenetic activation (3 minutes) before protein extraction. M5/4/3/2/1 n=1; WT/M<sup>3R</sup>: n=8.

(D) Immunoblot quantification of the normalized amounts of pATR (T1989), pRPA2 (S33) and pChk1 (S345) of n = 8 independent biological replicates. Welch's t-tests were applied (ns: non-significant; \*\*\*:  $p < 0.001$ ).

(E) Time course analysis of WT and M<sup>3R</sup> TopBP1<sup>opto</sup> focus size and turnover after illumination with 488 nm blue light (3 min, blue bulb). Coverslips were removed from the illuminated dishes at the indicated time points post illumination. TopBP1<sup>opto</sup> is visualized in the red channel and DNA is stained with Hoechst (blue channel). Scale bars: 10  $\mu$ m. The "0 min" timepoint (fixation right after illumination) was used to quantify the mean focus area of WT and M<sup>3R</sup> TopBP1<sup>opto</sup> condensates (panel F).

(F) *Superplot* quantifying WT and M<sup>3R</sup> TopBP1<sup>opto</sup> condensate area (pixels<sup>2</sup>) at the t=0 min timepoint of panel E. n=3 x 2000 foci were analyzed per condition and the plot shows the pool of the 3 biological replicates (yellow, green, blue). Data distribution is displayed as a half-violin plot on the right-hand side of the dotplots. The means  $\pm$  standard deviations (s.d.) are displayed on the graph. Welch's t-tests were applied (ns: non-significant).

(G) *Superplot* quantifying WT and M<sup>3R</sup> TopBP1<sup>opto</sup> condensate turnover shown in panel E in 3 independent biological replicates (yellow, green, blue). The plot shows the number of mCherry foci per nucleus at the different timepoints. Number of analyzed nuclei: WT no light: 2102, WT 0: 3742, WT 5: 3686, WT 10: 4016, WT 15: 3899, WT 20: 3570, M<sup>3R</sup> no light: 1627, M<sup>3R</sup> 0: 3866, M<sup>3R</sup> 5: 3843, M<sup>3R</sup> 10: 4090, M<sup>3R</sup> 15: 3761, M<sup>3R</sup> 20: 4118. Data are plotted as means (displayed on graph) with SEMs. Mann-Whitney tests were applied (ns: non-significant, \*\*\*:  $p < 0.001$ ).

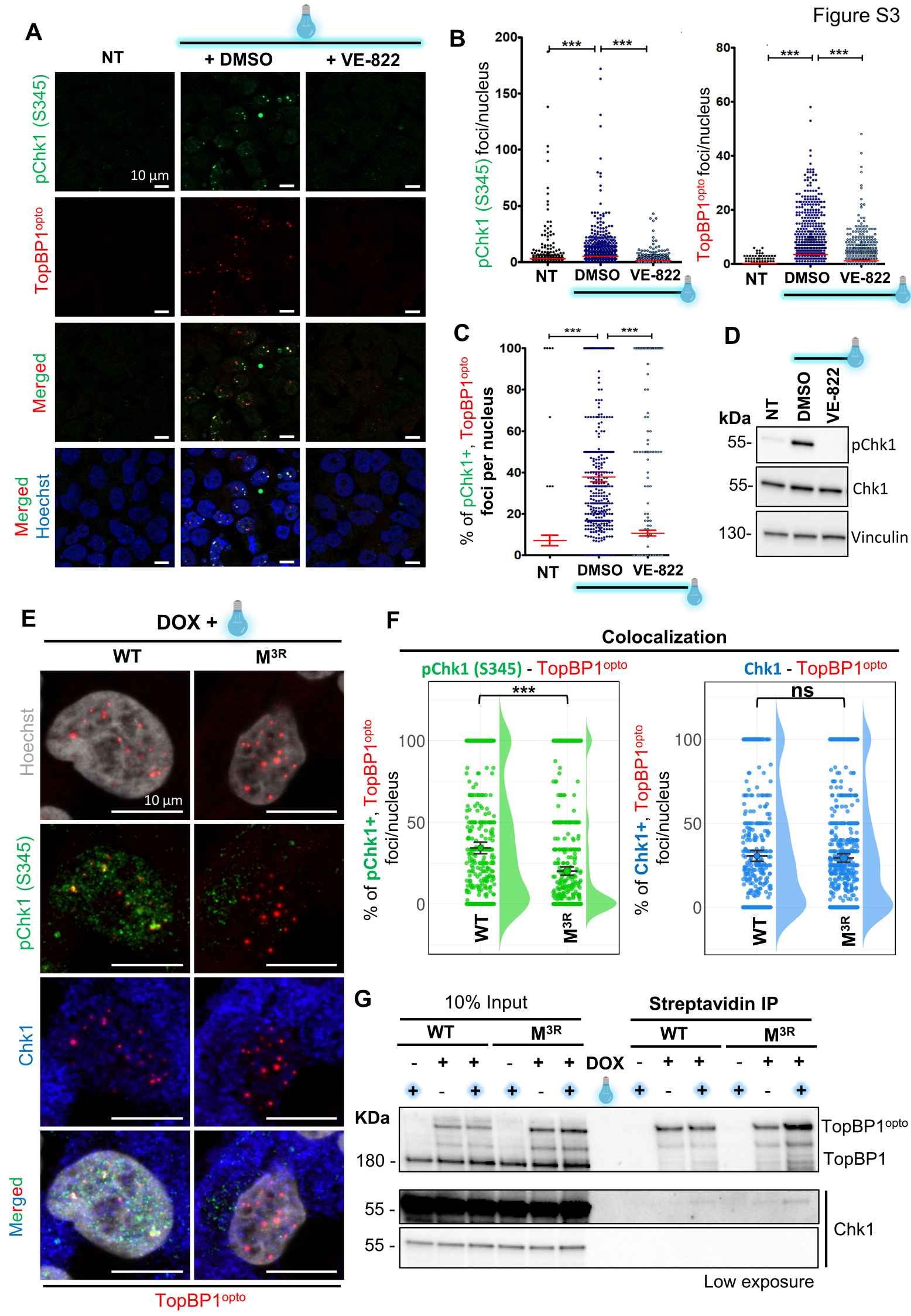


**Figure S3: pChk1 (S345) immunofluorescence signal around TopBP1 condensates is specific, and its loss in M<sup>3R</sup> is not due to a loss of proximity with total Chk1.**

(A) Representative micrographs of TopBP1<sup>opto</sup> condensates (red channel) and endogenous pChk1 (S345) (green channel). DNA is counterstained with Hoechst 33342 (blue channel). When indicated, TopBP1<sup>opto</sup> condensates were induced with 488nm light for 3 min (blue bulb), in cells pre-treated with the ATR inhibitor VE-822 (1  $\mu$ M, 1 h). NT: no treatment. Scale bars: 10  $\mu$ m. n=1.

(B) Quantitative dot plot analyses of the number of pChk1 (S345) foci and TopBP1 condensates per nucleus. Solid red lines represent the means and SEMs. Mann-Whitney tests were applied (ns: non-significant; \*\*\*: p < 0.001).

(C) Plot of the percentage pChk1 (S345) positive TopBP1 condensates per nucleus. Data are plotted as means with SEMs (red bars). n > 861 cells per condition. Mann-Whitney tests were applied (\*\*\*: p < 0.001).

(D) Immunoblotting, with the antibodies indicated, of whole-cell extracts from cells expressing WT TopBP1<sup>opto</sup>, harvested from the same plates as those from panels A-B.

(E) Representative micrographs of light (488nm)-treated (blue bulb) WT or M<sup>3R</sup> TopBP1<sup>opto</sup> cells expressing TopBP1<sup>opto</sup> constructs (red channel) and immunodetected for endogenous pChk1 (S345) (green channel) and total Chk1 (blue channel). DNA is counterstained with Hoechst 33342 (artificial gray channel). Scale bars: 10  $\mu$ m. n=1.

(F) *Superplot* analysis of the colocalizations between pChk1/TopBP1 or Chk1/TopBP1, as indicated. Object-based colocalization (percentage of pChk1 (S345) or total Chk1 positive TopBP1<sup>opto</sup> foci per nucleus). Total number of analyzed nuclei (>1 TopBP1<sup>opto</sup> focus) for pChk1 (S345): WT: 374 M<sup>3R</sup>: 568 ; for total Chk1 WT: 383 M<sup>3R</sup>: 646. Data distribution is displayed as a half-violin plot on the right-hand side of the dotplots. Data are plotted as means with SEMs. Mann-Whitney tests were applied (ns: non-significant; \*\*\*: p < 0.001).

(G) Immunoblots of TurboID proximity biotinylation of Chk1 in cells expressing WT or M<sup>3R</sup> TopBP1<sup>opto</sup> constructs. TopBP1 (<sup>opto</sup> and <sup>endo</sup>) are shown as controls. DOX: expression of TopBP1<sup>opto</sup> constructs. Blue bulbs: treatment by 3 min of 488 nm blue light.

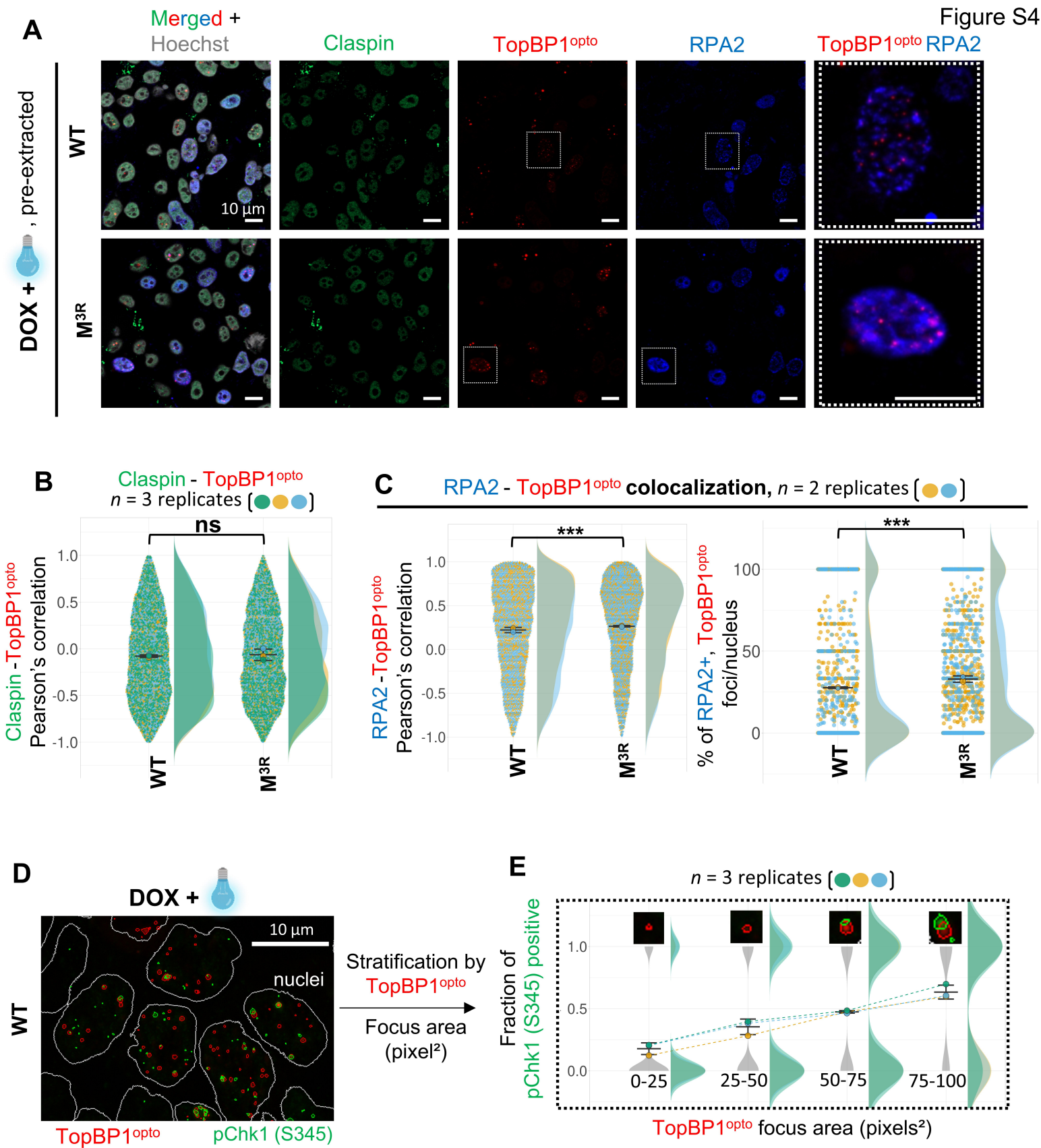


**Figure S4: Claspin and RPA2 are not responsible for the defect in Chk1 phosphorylation in M<sup>3R</sup> cells and TopBP1 focus size correlates with surrounding pChk1 (S345) phosphorylation.**

(A) Representative micrographs of light (488nm)-treated (blue bulb) WT or M<sup>3R</sup> TopBP1<sup>opto</sup> cells expressing TopBP1<sup>opto</sup> constructs (red channel) and immunodetected for Claspin (green channel) and chromatin-bound RPA2 (blue channel). DNA is counterstained with Hoechst 33342 (artificial gray channel). Scale bars: 10  $\mu$ m. n=2 (RPA2) - 3 (Claspin).

(B) *Superplot* analysis of the colocalization between Claspin and TopBP1<sup>opto</sup> (Pearson's correlation coefficient in TopBP1<sup>opto</sup> foci). n = 3 x 2000 foci. Data distribution is displayed as a half-violin plot on the right-hand side of the dotplots. Data are plotted as means with SEMs. Mann-Whitney tests were applied (ns: non-significant).

(C) *Superplot* analysis of RPA2 colocalization with TopBP1<sup>opto</sup> condensates. Left panel: pixel-based colocalization (Pearson's correlation coefficient in TopBP1<sup>opto</sup> foci). n=2 x 2000 foci. Data are plotted as means with SEMs and distribution is displayed as a half-violin plot on the right-hand side of the dotplots. Right panel: object-based colocalization (percentage of RPA2 positive TopBP1<sup>opto</sup> foci per nucleus). Total number of analyzed nuclei (>1 TopBP1<sup>opto</sup> focus): WT: 1125, M<sup>3R</sup>: 1518. Data are plotted as means with SEMs and distribution is displayed as a half-violin plot on the right-hand side of the dotplots. Mann-Whitney tests were applied (\*\*\*: p<0.001).

(D) Representative CellProfiler 4.2.1 image output showing the detection of TopBP1<sup>opto</sup> (red) and pChk1 (S345) (green) objects in light (488nm)-treated WT TopBP1<sup>opto</sup> cells. Nuclear masks are displayed in white. n=3.

(E) *Superplots* analysis of the fraction of TopBP1<sup>opto</sup> condensates positive for pChk1 (S345). 16,063 TopBP1 condensates were stratified in four size categories (0-25 ; 25-50 ; 50-75 ; 75-100 pixels<sup>2</sup>). Half-violin plots are displayed to facilitate the visualization of data distribution. Representative objects are displayed above the corresponding size categories.

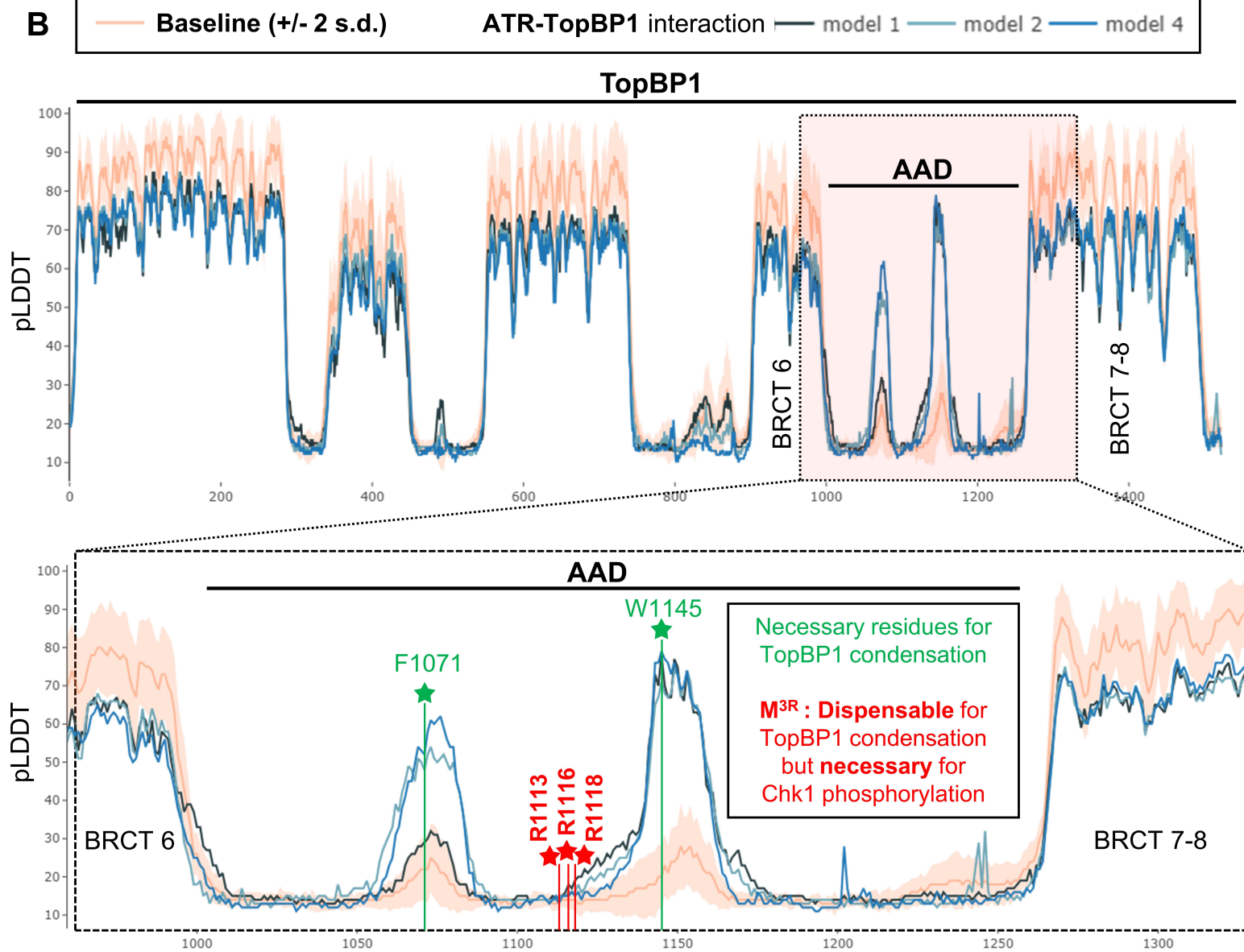
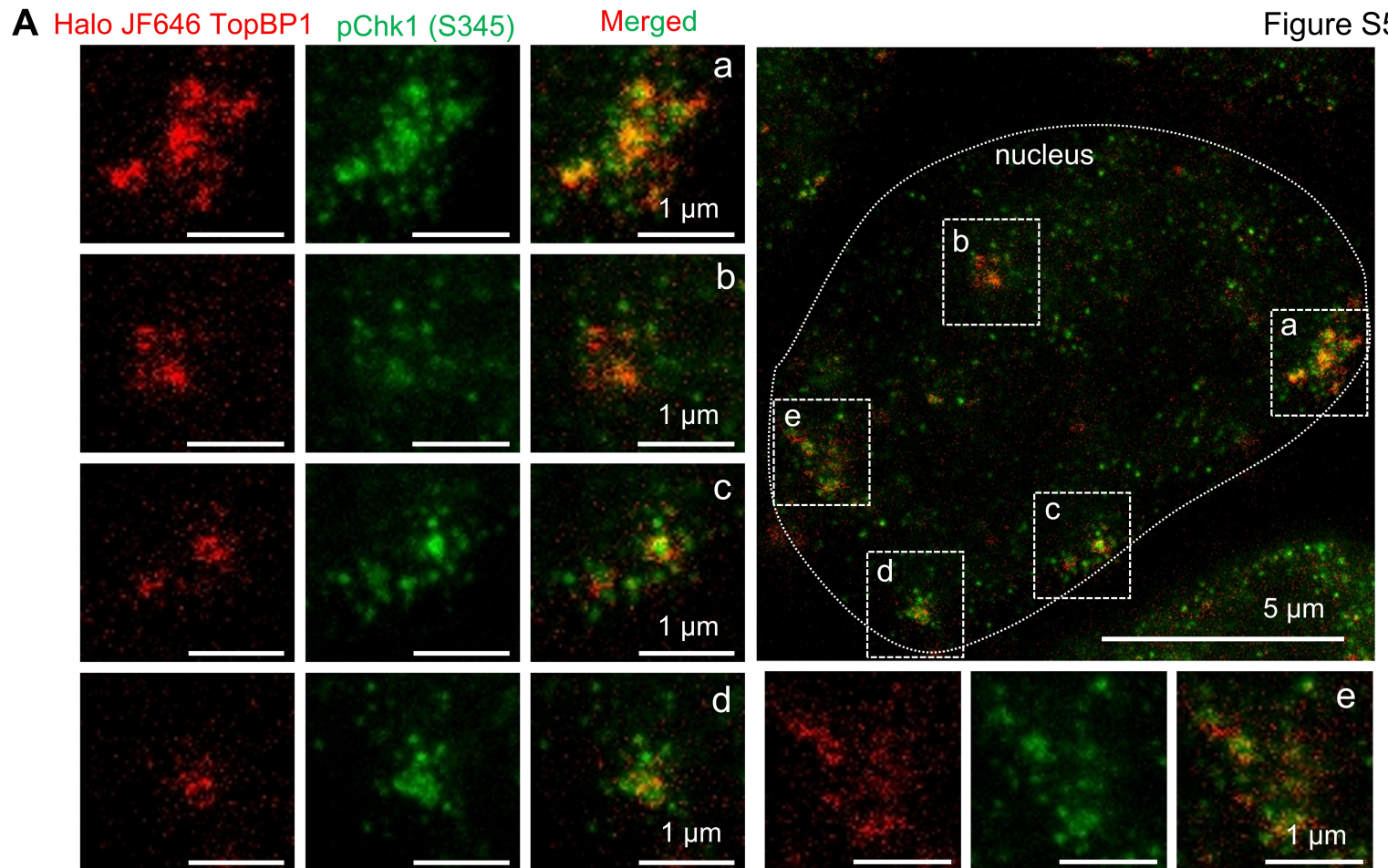


Figure S5

**Figure S5: Chk1 is phosphorylated at the interfaces of camptothecin-induced TopBP1<sup>Halo</sup> condensates & TopBP1 AAD structural predictions upon association with ATR.**

(A) Representative STED images of endogenous TopBP1<sup>Halo</sup> condensates stained live with JF646 (red channel) and pChk1 (S345) revealed by indirect immunofluorescence (green channel) from cells treated with camptothecin (1  $\mu$ M) for 1 hour. Scale bars are indicated (1  $\mu$ m left panels, 5  $\mu$ m right panels). a, b, c, d and e are magnifications of the corresponding sub-nuclear regions in the main, left panel.

(B) Above: Plots of pLDDT (predicted local distance difference test) of TopBP1 alone (baseline, orange) or interacting with ATR (3 models) generated on predictomes.org based on AlphaFold-Multimer (AF-M) deep learning system. The ATR Activating Domain (AAD) and BRCT6/7-8 are displayed. Below: Zoom on the AAD region (black dotted lines). Amino acids affecting TopBP1 condensation are displayed in green (F1071 and W1145)<sup>23</sup>. M<sup>3R</sup> mutated arginines (R1113, R1116 and R1118) presented in this work are displayed in red.

**Table S1:** Oligonucleotides used in this study. Related to Key Resources Table and Method Details.

Oligonucleotides	Sequence
Mutagenic primer M3R step1	gacagcactcgctctgctgccagtgaggagcaagtgagtcctagaggcactg
Mutagenic primer M3R step 2	cgctctgctgccagtgaggagcaagtgagtcctagaggcactg
Mutagenic primer M1	tctcagctgtgtcttcagcaaaggatgatgagcca
Mutagenic primer M2 step 1	gtgaaacccaagggcaggcgacttcctttcaagaag
Mutagenic primer M2 step 2	cagaggacttccttcagcaagtggttgtaacagcgc
Mutagenic primer M3	ccaagggcagagggcttccttgcaagaagtggttgta
Mutagenic primer M4	gcgcatcttcaaccgctgacagcactcgc
Mutagenic primer M5	cactcgctctgctcgcgctggacgaagtagagtc
Mutagenic primer S1273A	gaagaattaaaaaacagtacatatttcagttagcatctctgaatcctcaag
Mutagenic primer R1280Q	ttatcatctctgaatcctcaagaacaaattgactattgtcatctgattgaga
Mutagenic primer R1314Q	gttgtgggacatccacttcaaacgagaagtatttagcc